Cloud-Radiation Interactions and their Contributions to Convective Self-Aggregation

K. N. Pope[1], C. E. Holloway[1], T. R. Jones[1], T. H. M. Stein[1]

[1]Department of Meteorology, University of Reading

Key Points:

- The normalized FMSE variance budget is a consistent framework to study aggregation at all SSTs
- Radiative interactions with high cloud & water vapor drive aggregation and are sensitive to SST
- Longwave interactions reduce as model grid spacing is decreased, helping slow aggregation

Corresponding author: Kieran Pope, k.n.pope@pgr.reading.ac.uk

Abstract

This study investigates the direct radiative-convective processes that drive and maintain aggregation within convection permitting elongated channel (and smaller square) simulations of the UK Met Office Unified Model (UM). Our simulations are configured using three fixed sea surface temperatures (SSTs) following the radiative-convective equilibrium model intercomparison project (RCEMIP) protocol. By defining cloud types based on the vertical distribution of condensed water, we study the importance of radiative interactions with each cloud type to aggregation. We eliminate the dependence of the vertically-integrated frozen moist static energy (FMSE) variance budget framework on SST by normalizing FMSE between theoretical upper and lower limits based on SST.

The elongated channel simulations reach similar degrees of aggregation across SSTs, despite the contributions of normalized shortwave and longwave interactions decreasing with SST. High-cloud longwave interactions are the main drivers and maintainers of aggregation. Their influence decreases with SST as high clouds become less abundant. This SST-dependence is consistent with changes in grid spacing and RHcrit, however the magnitude of high-cloud longwave interactions is likely reduced as grid spacing and RHcrit are reduced. Both factors tend to decrease condensed water path and cloud top height, decreasing the anomalous longwave heating rates of these clouds. Shortwave interactions with water vapor are key maintainers of aggregation and are dependent on SST and the degree of aggregation itself. The analysis method used provides a new framework to compare the effects of radiative-convective processes on self-aggregation across different SSTs and model configurations in order to improve our understanding of self-aggregation.

Plain Language Summary

The spontaneous clustering of rainstorms (termed convective self-aggregation) is a common feature in weather and climate models. The amount of aggregation has a large influence on both weather and climate, so being able to understand how aggregation develops and how it is affected by a warming climate is important in both weather and climate modeling. Previous studies have shown that interactions between convection and radiation (both solar radiation and thermal radiation) are crucial for driving and maintaining aggregation. This study provides a detailed analysis into the key radiative-convective interactions that influence aggregation within simulations of the Met Office Unified Model. We assess their sensitivities to the model's sea surface temperature (SST), grid spacing, and critical cloud formation humidity. We find that the contribution of radiative-convective interactions to aggregation decreases as the SST is increased because the amount of high cloud decreases, and because the difference in absorption of solar radiation between humid and dry regions becomes less significant for aggregation. Decreasing both the model grid spacing, and the model's critical cloud formation humidity has the effect of decreasing the magnitude of the cloud interactions with thermal radiation, leading to a hypothesized slowing of the rate of aggregation.

1 Introduction

Weather over the tropical oceans is dominated by convection. The tropical atmosphere is in an approximate equilibrium between atmospheric radiative cooling and convective heating called radiative-convective equilibrium (RCE) (e.g. Arakawa & Schubert, 1974). With radiative cooling of the free troposphere, consistently high surface temperatures, and an abundant supply of moisture, convection occurs in an attempt to neutralize conditional instability, resulting in strong rainstorms. This convection can form a wide variety of structures with a great range of spatial and temporal scales depending on the state of convective organization. Structures can range from individual cumulonimbus clouds, to squall lines, mesoscale convective systems (MCSs), tropical cyclones, and the Madden-

Julian Oscillation (MJO) (Madden & Julian, 1971; Houze, 2004; Nakazawa, 1988; Mapes & Houze, 1993). The degree of aggregation affects the environment of both the convective and surrounding subsiding regions (e.g. Wing & Emanuel, 2014), as well as global-scale circulations (Arnold & Randall, 2015) and climate (Coppin & Bony, 2018).

There are many processes that cause convective organization, including convection within equatorial waves (Kiladis et al., 2009), organization along fronts, sea surface temperature (SST) hotspots, land and orography. Another process has been termed convective self-aggregation: a process, first identified in idealized models, by which convection spontaneously becomes clustered despite homogeneous initial conditions and forcing (e.g. Wing et al., 2017). Self-aggregation has been the focus of many recent studies, the majority of which have used idealized simulations of radiative convective equilibrium to further understand the processes that cause this phenomenon (Held et al., 1993; Bretherton et al., 2005; Muller & Held, 2012; Wing & Emanuel, 2014). A review of self-aggregation in numerical models has been published by Wing et al. (2017). Despite self-aggregation being first recognized in these idealized numerical models, key processes that drive self-aggregation are indeed relevant to the real atmosphere (Holloway et al., 2017).

We use the spatial distribution of frozen moist static energy (FMSE) as a framework to study aggregation (Wing & Emanuel, 2014). FMSE, or h, is given by

$$h = c_p T + gz + L_v q_v - L_f q_i \tag{1}$$

where c_p is the specific heat of dry air at constant pressure, T is temperature, g is the gravitational acceleration, z is the height above the surface, L_v is the latent heat of vaporization, q_v is the water vapor mixing ratio, L_f is the latent heat of fusion and q_i is the condensed ice mixing ratio.

The density-weighted vertical integral of FMSE is only affected by radiation, surface fluxes and advection. FMSE is approximately conserved, but redistributed under convective processes. As convection becomes more clustered, the horizontal variance in vertically integrated FMSE increases. A budget equation for the rate of change of vertically integrated FMSE shows that the horizontal variance in vertically integrated FMSE is driven by feedbacks with radiation, surface fluxes and advection. Many studies have shown the feedbacks between FMSE and both shortwave and longwave radiation are the key drivers and maintainers of aggregation (e.g. Holloway & Woolnough, 2016), and interactive radiation in models is essential for aggregation to occur (Bretherton et al., 2005; Muller & Bony, 2015).

Muller and Held (2012) find that it is the longwave cooling effect of low clouds within dry regions that is responsible for the onset of self-aggregation. The resultant circulation driven by the radiative cooling drives an upgradient transport of FMSE, which increases the variance of FMSE. They find the sensitivity of self-aggregation to domain size and resolution to be a result of the sensitivity of low cloud distributions within the model. Once the convection is aggregated, the longwave cooling effect of low clouds is not necessary to maintain aggregation (Muller & Held, 2012; Muller & Bony, 2015). During the mature phase of aggregation, the reduced longwave cooling of high clouds within high-FMSE regions becomes the dominant feedback maintaining aggregation (Wing & Emanuel, 2014).

Wing and Emanuel (2014) note the importance of the shortwave radiative feedback due to the increased absorption of shortwave radiation within high FMSE regions compared to low FMSE regions, increasing the FMSE variance. They also note that dry regions initially have anomalously strong radiative cooling, resulting in a positive longwave feedback, whereas at later times, the dry regions amplify, becoming dryer, which decreases

low-level emissivity. Anomalous longwave heating then develops at low levels to the extent that the column longwave heating anomaly becomes positive.

The contributions from cloud-radiation interactions to convective self-aggregation are generally implied in these previous studies, but a detailed analysis considering the role of specific cloud types is missing. With both the horizontal and vertical distribution of clouds being one of the largest sources of variability amongst RCE simulations (Wing et al., 2020), a detailed investigation into the role of specific cloud types on self-aggregation may help in explaining the variability of self-aggregation amongst RCE simulations and the consequential implications for climate sensitivity.

This study investigates the direct radiative-convective processes that are important to self-aggregation, and their sensitivity to SST within elongated channel simulations of the UK Met Office Unified Model (UM) version 11.0. We then investigate how the SST-dependent convective features and their radiative interactions are affected by model grid spacing and treatment of subgrid condensation using smaller square domains. Our simulations are configured using three fixed sea surface temperatures (SSTs) following the radiative-convective equilibrium model intercomparison project (RCEMIP) protocol. The model setup is described in section 2.1. We use a budget equation for the variance of normalized vertically-integrated FMSE which minimizes the SST dependence of horizontal FMSE variance (section 2.2). This allows us to compare how the impacts of radiative feedbacks on aggregation change with SST. We categorize cloud types based on the vertical distribution of condensed water path (CWP) and analyze their radiative interactions that impact aggregation. This categorization is shown in section 2.3.

We first analyze how convection aggregates within the three channel simulations in section 3, and show how the FMSE budget terms vary with time and SST. We then analyze the radiative feedbacks responsible for maintaining aggregation in the large domain and compare how SST affects these feedbacks in section 4. Then, we look at the dominant radiative feedbacks during the early stages of aggregation and see how they change with time (section 5). Finally, we investigate how these radiative interactions are affected by both resolution and the critical humidity threshold for condensation to occur (RHcrit), using smaller domains with lower grid spacing (section 6). A summary and conclusions is presented in section 7.

2 Methods

2.1 Model Configuration

In this study, we use the UK Met Office Unified Model version 11.0 to run simulations of RCE at three fixed SSTs of 295, 300 and 305 K. This study mainly focuses on convection within the "*LARGE*" domain, however we also use three other domains: "*SMALL*", "*SMALL_HI*", and "*SMALL_RHCRIT*", to assess how the radiative properties of clouds are affected by grid spacing and RHcrit.

The *LARGE* and *SMALL* simulations have been configured following the radiative-convective equilibrium model intercomparison project (RCEMIP) protocol set out by Wing et al. (2018). The *LARGE* domain is 6048 km $\times$ 432 km in size with a 3 km horizontal grid spacing and the *SMALL* domain is 100 km $\times$ 100 km with a 1 km grid spacing. The *SMALL_HI* domain is also 100 km $\times$ 100 km in size but has a horizontal grid spacing of 0.1 km.

The *LARGE*, *SMALL*, and *SMALL_HI* simulations all have a uniform RHcrit value of 0.99 across the entire domain. The value of RHcrit should depend on the dimensions of the grid box, with coarser grid boxes requiring a lower RHcrit to yield realistic cloud amounts. Our value is too high to yield realistic low cloud distributions (Morcrette, 2013) particularly for our coarser grid spacings. To see the effects of a more realistic RHcrit,

we used another set of simulations that are identical to our *SMALL* simulations but for an RHcrit distribution used in the UK Met Office UKV model. Here, RHcrit is set to 96% in the lowest layers and decreases steadily to 80% at 900 m. RHcrit is then maintained at 80% above this level.

The RCEMIP protocol states that large-domain simulations for a given SST are initialized using the equilibrium soundings of the corresponding small-domain simulations, providing aggregation does not occur in the small-domain. In our case, the *SMALL* simulations showed signs of self-aggregation, therefore, our *LARGE* simulations are initialized from a corresponding small-domain simulation with homogenized radiation, which showed no sign of aggregation. Note that there was a mistake in the initialization of the *LARGE* simulations, in that the initial humidity profile is out by a density factor. With density close to unity in the regions with highest absolute humidity, and with the 2-day spin-up period neglected in the conclusions of our analysis, we believe this error will not have an impact on our conclusions.

The simulations are configured over an ocean, without rotation, and have a fixed solar insolation of 409.6 W m^{-2} (the tropical annual mean). The *LARGE* domain simulations are run for 113 days, the *SMALL* simulations are 124 days, the *SMALL_HI* simulations are 54 days, and the *SMALL_RHCRIT* simulations are 123 days. 3D data are produced every 6 hours, which is the temporal resolution of our analysis.

The science configuration of our simulations is based on the tropical Regional Atmosphere and Land (RAL1-T) configuration (Bush et al., 2020). However, we use the Smith sub-grid cloud scheme (Smith, 1990) rather than the PC2 scheme (Wilson et al., 2008). With our simulations configured over an ocean, the land settings of RAL1-T are not used. The simulations use explicit convection set over a flat, Cartesian grid, with biperiodic boundary conditions, using a vertical sigma-z-coordinate Charney-Philips staggering (Charney & Phillips, 1953). We use a 60 s time step for the *LARGE* simulations, a 30 s time step for the *SMALL* and *SMALL_RHCRIT* simulations, and a 5 s time step for the *SMALL_HI* simulations. The dynamical core uses a semi-implicit, semi-Lagrangian scheme that solves the non-hydrostatic, fully compressible, deep-atmosphere equations of motion (Wood et al., 2014).

The radiation scheme used is the Suite of Community Radiative Transfer codes based on Edwards and Slingo (SOCRATES) (Edwards & Slingo, 1996) with the full radiation being computed at 15-minute time steps and the simplified radiation at 5-minute time steps. The boundary layer scheme used is based on that described in Lock et al. (2000) with updates described in Walters et al. (2019). The subgrid turbulence scheme is based on Smagorinsky (1963) with multiple extensions from Lock et al. (2000). We use Rayleigh damping of all prognostics in a "sponge layer" in the upper levels of the model, with the damping timescale following an exponential function of height from 24-40 km. The microphysics used is a single-moment scheme based on Wilson and Ballard (1999).

2.2 Normalization of FMSE

Using the variance of vertically-integrated FMSE (var($\widehat{h}$)) as the metric for comparing aggregation across different SSTs has its pitfalls as it is very strongly dependent on temperature. To account for this, we normalize vertically-integrated FMSE between a theoretical upper and lower limit using the formula:

$$\widehat{h}_n = \frac{\widehat{h} - \widehat{h}_{min}}{\widehat{h}_{max} - \widehat{h}_{min}} \tag{2}$$

where hats ($\widehat{\ }$) denote a density-weighted vertical integral, and $\widehat{h}_{max}$ and $\widehat{h}_{min}$ are upper and lower limits of $\hat{h}$ for a given SST. $\widehat{h}_{max}$ is defined as the vertically-integrated FMSE

of a fully saturated moist pseudoadiabatic profile from the surface to the tropopause, plus the integrated FMSE of the initial profile for the *LARGE* simulations above the tropopause. For $\widehat{h}_{min}$, the vertically-integrated FMSE of a dry adiabatic profile with zero moisture is used within the troposphere, and again, integrated FMSE above the tropopause from the initial profile is added. The SST is used as the temperature at sea-level pressure to initiate both adiabatic profiles. The tropopause is defined as the lowest level in the initial profile at which the lapse rate decreases to 2°C/km or less. The values of $\widehat{h}_{max}$ and $\widehat{h}_{min}$ are shown in Table 1, along with the height and pressure of the tropopause and the integrated FMSE above it. With less than 15% of the mass-weighted integral of $\widehat{h}_{max}$ and $\widehat{h}_{min}$ coming from the FMSE above the tropopause, the way we define the tropopause has little effect on these limits and does not impact our conclusions.

Table 1. Values of $\widehat{h}_{max}$ and $\widehat{h}_{min}$ for each SST used in equation (2) to normalize $\widehat{h}$.

SST (K)	$\widehat{h}_{min}$ (GJm^{-2})	$\widehat{h}_{max}$ (GJm^{-2})	Tropopause Pressure (hPa)	Tropopause altitude (km)	$\widehat{h}$ above tropopause (GJm^{-2})
295	3.219	3.628	92.0	16.6	0.458
300	3.270	3.837	100.4	16.4	0.486
305	3.315	4.059	100.9	16.8	0.486

The relative importance of different processes to changing the variance of FMSE can be analyzed using the budget equation derived by Wing and Emanuel (2014):

$$\frac{1}{2}\frac{\partial \hat{h}'^2}{\partial t} = \hat{h}'LW' + \hat{h}'SW' + \hat{h}'SEF' - \hat{h}'\nabla_h.\hat{\mathbf{u}h} \tag{3}$$

where SEF is the surface enthalpy flux, made up of the surface latent heat and sensible heat fluxes, $\nabla_h.\hat{\mathbf{u}h}$ is the horizontal divergence of the $\widehat{h}$ flux, primes ($'$) indicate local anomalies from the instantaneous domain-mean, and LW and SW are the net atmospheric column longwave and shortwave heating rates.

This equation is suitable for comparing the importance of different $\widehat{h}$ feedbacks to aggregation within models at the same SST. However, due to the strong dependence of $\text{var}(\widehat{h})$ to SST, this equation cannot be used to analyze how the importance of these feedbacks to aggregation change with SST. To enable fair comparisons of aggregation with SST, we frame our analysis using a budget of the horizontal variance of $\widehat{h}_n$. By following the budget equation derivation by Wing and Emanuel (2014) and using $\widehat{h}_n$ instead of $\widehat{h}$, equation 3 becomes:

$$\frac{1}{2}\frac{\partial \widehat{h}_n'^2}{\partial t} = \hat{h}_n'LW_n' + \hat{h}_n'SW_n' + \hat{h}_n'SEF_n' - \hat{h}_n'\nabla_h.\hat{\mathbf{u}h}_n \tag{4}$$

Here, each of the three normalized flux anomalies on the RHS (LW_n', SW_n', and SEF_n') is equal to the original flux anomaly in equation 3 divided by the difference between $\widehat{h}_{max}$ and $\widehat{h}_{min}$. The derivation of this equation is shown in the appendix.

2.3 Cloud Classification Scheme

The cloud classification scheme used in this study is based on the classification scheme outlined by Hill et al. (2018), which classifies clouds using the vertical structure of condensed water content. In their study, they define high cloud to be located above 440 hPa and low cloud to be below 680 hPa with mid-level cloud being anything in between. Clouds spanning two or more levels have their own categories, and they distinguished between

clouds that are contiguous or not between these layers. In total there are 12 cloud categories. In this study, a minimum condensed water content of 10^{-6} kg m^{-3} is used as a cloud threshold. This is the approximate limit below which the difference between the longwave and shortwave heating rates of clear-sky (without condensed water) and all-sky radiative transfer calculations are almost negligible (analysis not shown).

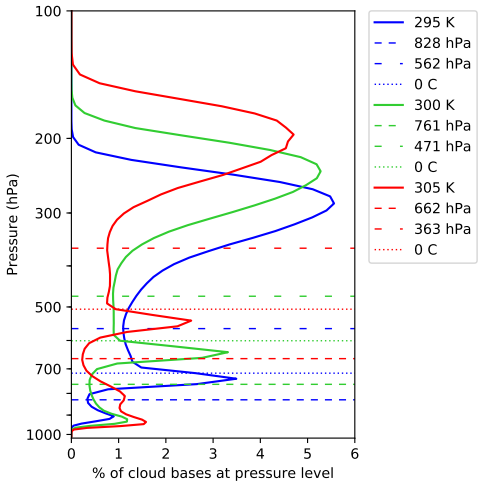

Figure 1. Cloud base distributions throughout each of the *LARGE* domain simulations. The lower and upper pressure thresholds (P1 and P2) for each SST are shown in narrow and wide dashed lines respectively, and the mean freezing level is shown in dotted lines.

With the depth of the troposphere being strongly dependent on temperature, so too is the vertical distribution of cloud. By analyzing the vertical distribution of cloud bases throughout the *LARGE* domain simulations, it was apparent that these pressure thresholds should also vary with temperature. Distributions of cloud base pressures for each of the *LARGE* simulations are shown in Figure 1. The cloud base at a given column is calculated as the lowest-altitude pressure at which the condensed water content exceeds 10^{-6} kg m^{-3} (the distribution shown, therefore, does not account for additional cloud bases above the lowest base). The profiles of cloud base have very similar features for each SST, with two consistent local minima within each distribution. These two minima will be the chosen pressure thresholds that define the cloud types throughout this study. The lower-level threshold is defined as the first cloud base distribution local minimum below the freezing level. The upper-level threshold is the highest-altitude cloud base distribution local minimum. The lower-level thresholds (P1), and the upper-level thresholds (P2) for each SST are shown in figure 1.

Rather than using all 12 cloud types used by Hill et al. (2018), we have merged the cloud types that were only distinguishable by whether or not they are vertically contiguous. We analyzed radiative heating rates for all 12 cloud types, and found that the types we have merged have similar heating rates for a given CWP (not shown). The merged cloud types also have similar $\widehat{h}$ distributions, meaning they will have similar radiative interactions for a given CWP. The main differences between the individual cloud types is their CWP distributions, with the contiguous types tending to have higher CWPs. We end up with the 8 cloud types used in this study, including Clear regions. A schematic of the categories is shown in Figure 2.

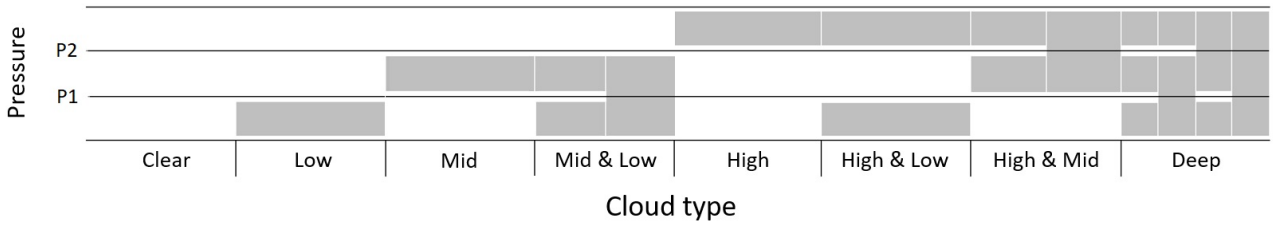

Figure 2. Schematic of the categories used in this study. P1 and P2 are the lower and upper-level pressure thresholds respectively. The shading is contiguous across rows if the cloud type extends across multiple layers.

3 Aggregation within the *LARGE* Domain

We briefly consider the evolution of convective aggregation in the *LARGE* domain at the different SSTs. Hovmöller plots for each simulation are shown in Figure 3 using $\widehat{h}_n$ as a proxy for moist convective regions. The Hovmöller diagrams were made by averaging $\widehat{h}_n$ along the short axis of the domain. The evolution of the variance of column-integrated FMSE for each SST is shown in Figure 4a. Visually, this metric has a strong correlation with SST since a warmer atmosphere is able to contain exponentially more water vapor via the Clausius-Clapeyron relationship, so there will be a larger difference in FMSE between the dry and moist regions. Normalization allows for fair comparisons of aggregation across all SSTs whilst using the FMSE variance framework. $\mathrm{Var}(\widehat{h}_n)$ is a consistent metric for each SST, with values less than 10^{-4} corresponding to uniformly scattered convection, and values greater than 10^{-3} corresponding to strong convective aggregation.

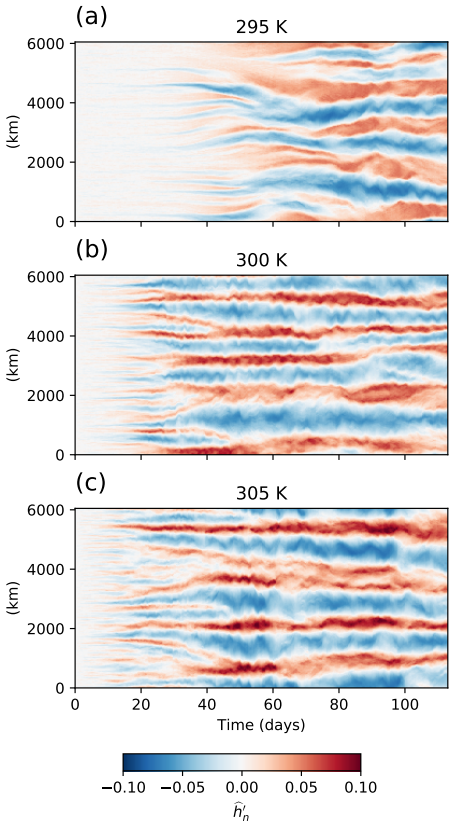

Figure 3. Hovmöller diagrams of $\widehat{h}_n$ for each SST for the *LARGE* domain runs. $\widehat{h}_n$ is averaged across the short axis of the domain.

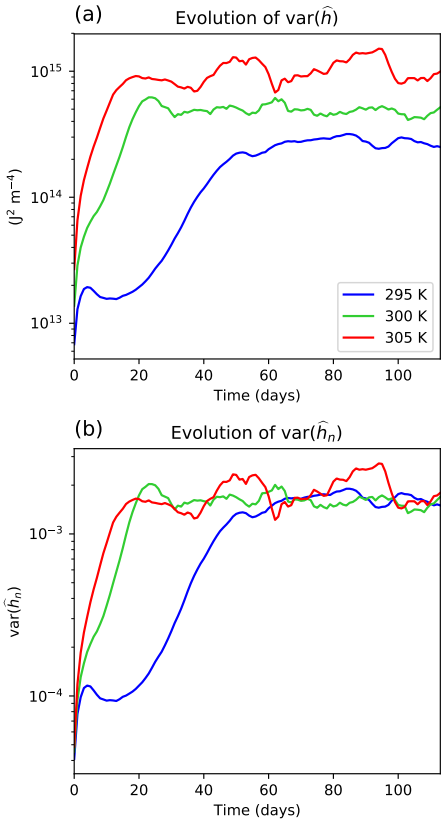

Figure 4. Daily means of the (a) spatial variance of $\widehat{h}$, and (b) variance of $\widehat{h}_n$, for each SST for the *LARGE* domain.

The variance of $\widehat{h}_n$ is shown in Figure 4b and indicates that the degree of aggregation reaches a similar level at the end of the three simulations. This is expected because the organization of convection visually appears similar at the end of the simulations, verifying this metric is consistent across the SSTs we have used. This gives us an idea of the state of aggregation within the domain, with higher values correlating with a more aggregated state. However, the points in time at which the variances of $\widehat{h}$ level off appear to occur earlier than the points in time at which the convection becomes the

most clustered (compare Figures 3 and 4). Once the moist regions no longer get moister, and the dry regions no longer become drier, $\mathrm{var}(\widehat{h})$ will reach its maximum value. It may only take around the timescale of a convective cell for a column to reach the upper limit of $\widehat{h}$, however it takes much longer for the driest regions to reach the lower limit. The drying of the dry regions may be on the same timescale as the subsidence timescale; the time it takes for the very dry air near the tropopause to descend throughout the depth of the free troposphere. $\mathrm{Var}(\widehat{h})$ correlates strongly with aggregation, although it does not necessarily indicate how clustered the convection is once the maximum variance is reached.

Beginning with the 295 K SST simulation, scattered convection initiates rapidly and homogeneously within the first five hours across the entire domain (not shown). After a couple of days, dry regions begin to develop within which deep convection is suppressed. These dry regions begin to grow in size and subsequently become drier. As the dry regions expand and merge, the moist regions become increasingly confined and become moister. The most prevalent dry regions are usually surrounded by the most intense convection. Dry regions continue to expand, constricting the moist regions until an approximate equilibrium state is reached after around day 70. In this fully-aggregated equilibrium state, four to five moist bands align along the short axis of the domain, separated by dry, mostly clear regions. This evolution is consistent with the majority of non-rotating large-domain simulations of RCE (Wing et al., 2017).

The aggregation process occurs much faster for the 300 K SST simulation. As soon as the convection initiates, numerous dry regions are simultaneously formed. These are far more abundant than within the 295 K simulation. They expand, merge, and become drier as the moist regions constrict, become moister, and precipitate intensely. The equilibrium aggregated state is reached by around day 50. For the 305 K SST simulation, dry regions develop within the first day and are as abundant as moist regions. As they expand, merge, and dry further, the convection aggregates very rapidly compared with the cooler simulations. However, the equilibrium stage is still reached around day 50. This progression of aggregation is consistent with other studies such as Wing and Cronin (2016), who use a wider and narrower channel domain of 12 288 km $\times$ 192 km with a 3 km grid spacing. They also find convection aligning into bands along the short axis, occurring at time scales similar to what we have seen in our simulations for the SSTs used. They observed the length scale of the convective bands decreasing with SST, which is less apparent in our simulations, with each of ours displaying four to five bands of deep convection. We likely do not see the same trend as in their simulations due to the less narrow domain of our simulations. However, it appears as though the moist bands in our simulations become narrower with increased SST.

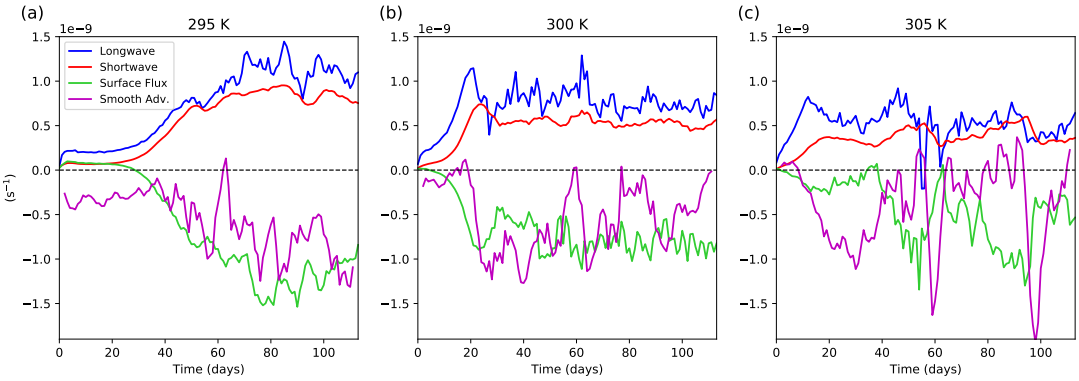

Figure 5. Domain-mean of RHS terms in equation (4) for (a) 295 K, (b) 300 K, (c) 305 K within the *LARGE* domain. Each point represents a daily mean of the term. The convergence term is calculated as a residual of the other terms and is a 5-day running average, shown to reduce noise.

The domain-mean values of the terms in the $\hat{h}_n'^2$ budget (equation 4) are shown in Figure 5. Where the terms are positive, they are contributing to an increase in var($\widehat{h}_n$), and hence encourage aggregation. The figure shows that within all of the *LARGE* simulations, the domain-means of the radiative terms are almost always positive. The longwave term is the dominant driver of aggregation at early times, and both the longwave and shortwave feedbacks maintain the aggregation in the mature phase. During the aggregating phase, the sum of all the terms on the RHS is generally positive, leading to an increasing var($\widehat{h}_n$) and increasing aggregation. The magnitude of all terms tends to increase as var($\widehat{h}_n$) increases since each term in the equation is a product that includes $\widehat{h}_n'$.

At early times, the advection term becomes increasingly positive with SST and may help explain why aggregation occurs faster within our warmer simulations. Once the equilibrium state is reached with the convection being fully aggregated, the radiative terms are balanced by the surface flux and advection terms. The magnitudes of both the longwave and shortwave radiative terms decrease with SST. The decrease in the radiative terms with SST is balanced by the decrease in magnitude of the (negative) surface flux and advection terms, resulting in the total variance of $\widehat{h}_n'$ being similar across all SSTs during the mature phase of aggregation.

4 Cloud-Radiative Interactions within the *LARGE* Domain

Interactions between radiation and cloud/moisture responses to convection have been shown to be crucial contributors to convective self-aggregation (e.g. Wing et al., 2017; Arnold & Putman, 2018). The aim of this study is to investigate and quantify the dominant direct cloud-radiative interactions that impact convective aggregation.

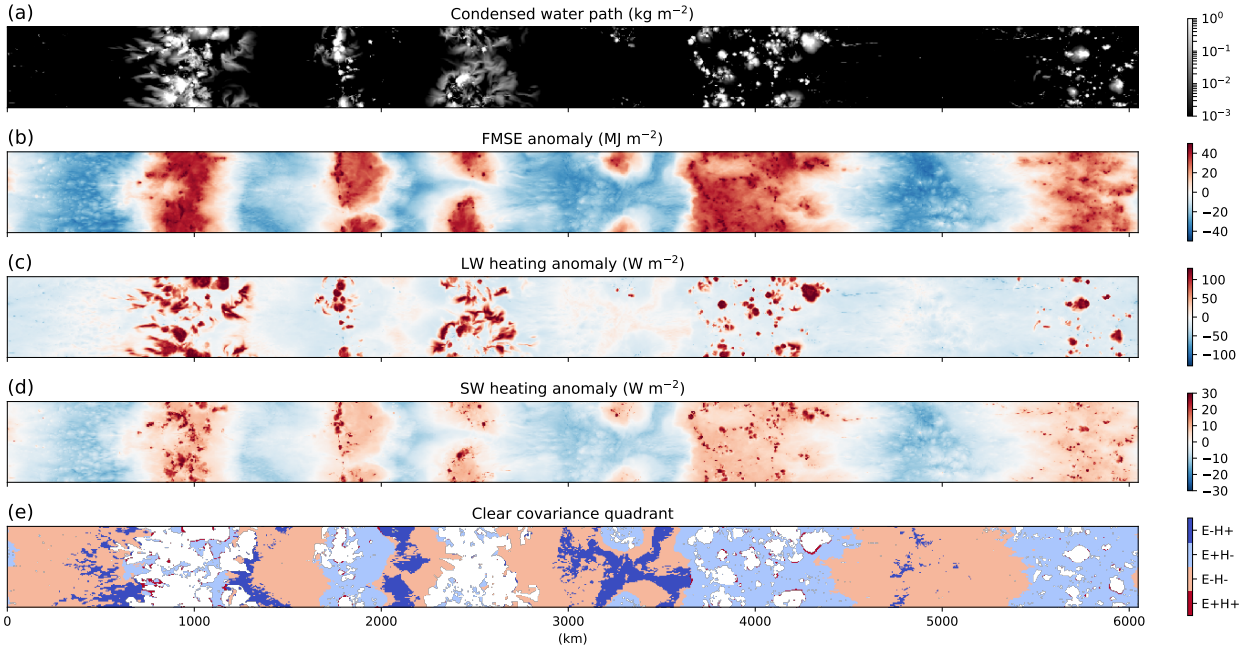

Figure 6. Maps of (a) condensed water path (kg m^{-2}), (b) instantaneous FMSE anomaly (MJ m^{-2}), (c) longwave heating anomaly (W m^{-2}), (d) shortwave heating anomaly (W m^{-2}), (e) Clear covariance quadrant (4.2) - note that clouds are colored white in (e). Snapshots taken at day 100 in the *LARGE* domain with SST = 300 K. Regions where the FMSE anomaly ("E") and radiative heating anomaly ("H") have the same sign contribute to increasing var($\widehat{h}$).

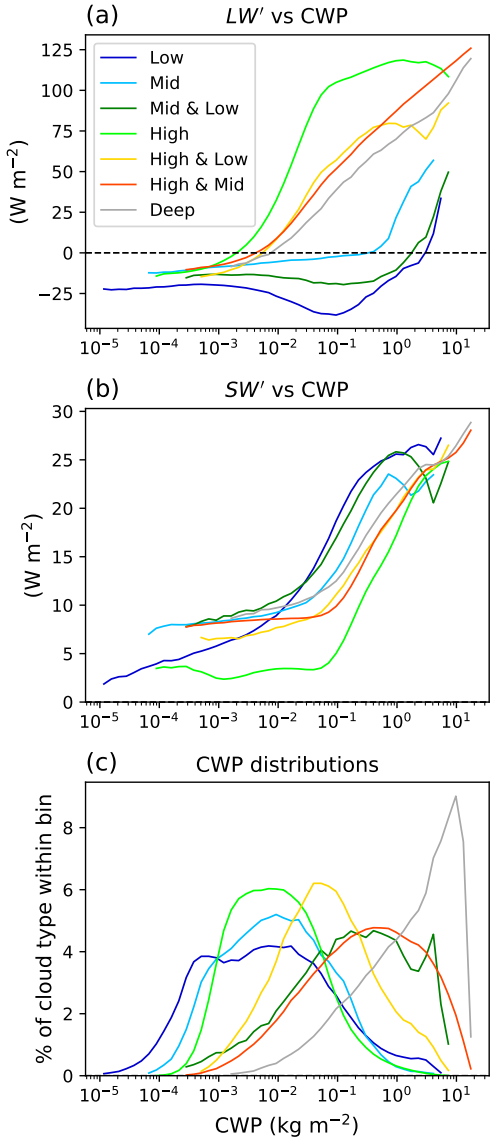

Figure 7. (a) Longwave and (b) shortwave radiative heating anomalies vs condensed water path for each cloud type, and (c) distributions of condensed water path for each cloud type. Data from the final 20 days of the *LARGE*, 300 K SST simulation. 50 bins are spaced logarithmically throughout the CWP range. The percentage shown in (c) is the percentage of each cloud type within a given bin.

Since both radiative anomalies and FMSE anomalies are calculated at each grid point, the instantaneous values of the radiative terms in equation (4) can also be calculated at each point across the domain. Then, by knowing the cloud type at each grid point, the contributions of each category to the domain-mean radiative terms can be found. With this approach, we study how the radiative feedbacks of the entire column of each cloud category contribute to the var($\widehat{h}_n$) tendency of the entire domain. Note that this approach does not describe the cloud-only effect, and since the anomalies of FMSE and radiation also depend on the domain-mean, var($\widehat{h}_n$) is not purely a local metric. We only consider the column-integrated cloud-radiative feedbacks here, although indirect radiative interactions with cloud are shown to be important via the generation of circulations (Muller & Bony, 2015; Holloway & Woolnough, 2016). Nevertheless, we find the approach to be a useful way to compare the relative importance of each cloud type's direct radiative contribution to self-aggregation across a range of SSTs.

From Figure 6a–d, it is clear that there is a very strong spatial correlation between $\widehat{h}'$ and the column shortwave heating anomaly, with CWP having the strongest relationship with the column longwave heating anomaly. To begin to quantify the longwave and shortwave heating effects of clouds, the mean radiative anomalies of each cloud type for a given CWP are shown in Figure 7a & b. The radiative heating in both the longwave and shortwave varies strongly with CWP. The cloud type is also a very important factor in the radiative anomalies, particularly in the longwave. For a given CWP, High clouds have the largest column longwave heating rates since they have low outgoing longwave radiation (OLR) and they also emit relatively little to the surface. Low clouds have warm tops and warm bases, so they effectively emit into space as well as to the surface, efficiently cooling the column. While Deep clouds emit weakly to space, their low, warm bases strongly emit towards the surface, placing their longwave heating rates in between High and Low clouds for a given CWP.

In the shortwave, each cloud type's heating rate increases with CWP, although this is largely due to increased shortwave absorption by water vapor within these columns (section 4.3). There is however some dependence on cloud type due to the high reflectivity of clouds. Water vapor is a very effective absorber of shortwave radiation and is mainly constrained to the warm lower atmosphere. High cloud columns have the lowest shortwave heating rates as they reflect radiation out of the column before the low-level water vapor has the chance to absorb it. Columns with Low clouds typically have the highest shortwave heating rates as their low vertical extent allows lots of shortwave radiation to be absorbed by water vapor. The radiation they reflect may also be absorbed by water vapor above the cloud.

The distributions of CWP for each cloud type are shown in Figure 7c. These distributions, paired with the dependence of the radiative anomalies on CWP, determine the mean radiative anomalies for each cloud category (domain-averaged heating rates of all categories are shown in Figure 9f). Despite the High clouds having the largest longwave heating rate for a given CWP, their CWP distribution peaks at around 0.01 kg m^{-2}, corresponding to a longwave heating anomaly of roughly 20 W m^{-2}. In contrast, the High & Mid cloud has a peak CWP around 0.5 kg m^{-2} corresponding to a longwave heating anomaly around 70 W m^{-2}. This results in High clouds having only the fourth largest domain-averaged longwave heating rates out of all categories.

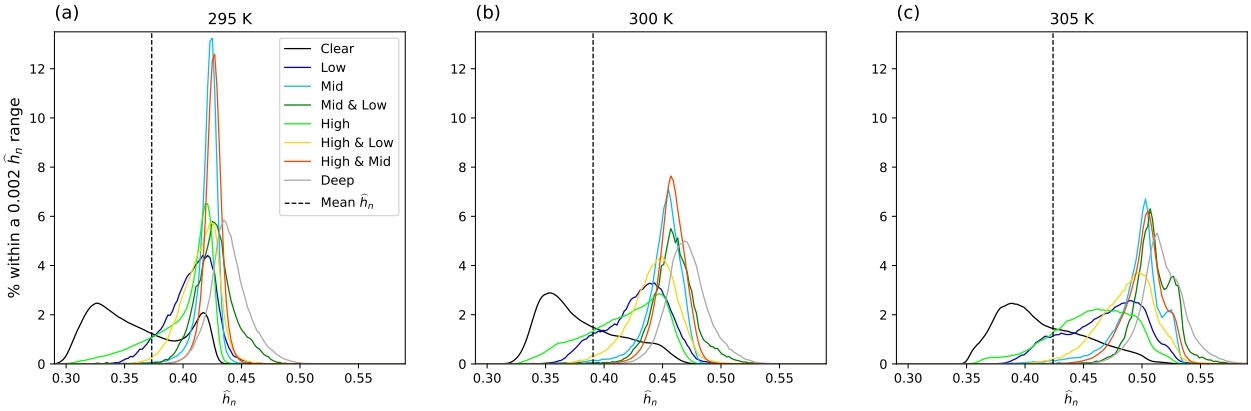

Figure 8. Distributions of $\widehat{h}_n$ for each cloud type for all SSTs within the *LARGE* domain during the final 20 days. The vertical dashed line indicates the domain-mean $\widehat{h}_n$ throughout the final 20-day period. Note that each curve is normalized individually.

Distributions of $\widehat{h}_n$ for the final 20 days of the *LARGE* simulations for each cloud category are shown in Figure 8. The vast majority of clouds occur within anomalously high $\widehat{h}_n$ regions, with only a few High and Low clouds occurring with negative $\widehat{h}'_n$. High clouds have the largest spread of $\widehat{h}_n$ out of all the cloud types as they can extend hundreds of kilometers away from the updraft, spanning a wide $\widehat{h}_n$ range. Low clouds occur within a broad span of $\widehat{h}_n$ as they can form under a wide range of conditions. At higher $\widehat{h}'_n$ regions, Low clouds form and may continue to develop into congestus and cumulonimbus, as the environment is favorable for deep convection. At lower $\widehat{h}'_n$ regions, descending motion throughout the free troposphere increases stability and reduces humidity, making the atmosphere unfavorable for deep convection, but shallow cumulus and stratocumulus may still form and persist atop the well-mixed boundary layer. The majority of the other cloud types are associated with deep convection, which only occurs within high $\widehat{h}'_n$ regions, where the environment is favorable for updraft development. Whilst the domain-mean $\widehat{h}'_n$ for the Clear regions is slightly negative, there is a very large spread in the distribution of $\widehat{h}_n$, with just under half of the Clear regions having positive anomalies.

As SST increases, the domain-mean $\widehat{h}_n$ increases slightly which may be a result of the increased moisture content of higher SST simulations, making the mean profile tend further away from a dry adiabat, in turn increasing $\widehat{h}_n$. However, with our analysis framework, we are not concerned about the absolute $\widehat{h}_n$ but rather the anomalies, which can be objectively observed by looking at the distance from the mean $\widehat{h}_n$ line in Figure 8. We find that the average $\widehat{h}_n$ anomaly for each cloud type increases with SST. This is likely a result of the decrease in the number of high-FMSE cloudy regions as SST increases (see Figure 9c). This brings the domain-mean $\widehat{h}_n$ towards the mean of the clear regions, making the higher $\widehat{h}$ of the cloudy regions more anomalous.

4.1 Longwave Cloud Interactions

The contribution of each cloud category to the radiative terms can be calculated by multiplying their mean covariance between the normalized radiative and $\widehat{h}$ anomalies by their cloud fraction. Figure 9a shows that it is the Clear, High, High & Mid, and Deep categories that have the largest contribution to the longwave term once the domain is fully aggregated, with the magnitude of their contributions being highly sensitive to SST. The contributions of the Low, Mid, Mid & Low and High & Low categories have a relatively insignificant contribution. To understand the magnitudes of the contributions of each cloud type to the longwave term, the constituents of the longwave term are shown in Figure 9b - f. The figure shows the $LW'_n \times \widehat{h}'_n$ covariance, and the fraction of each category. The mean LW'_n and $\widehat{h}'_n$ are also shown, as well as the non-normalized longwave anomaly. Note that the mean LW'_n multiplied by the mean $\widehat{h}'_n$ does not equal the mean $LW'_n \times \widehat{h}'_n$ covariance, although for most categories they are approximately equal. One notable exception is the $LW'_n \times \widehat{h}'_n$ covariance for the Clear regions at 305 K, which is negative, despite having both negative LW'_n and $\widehat{h}'_n$. This is discussed in section 4.2.

At all SSTs, and despite its relatively low $LW' \times \widehat{h}'$ covariance, the High cloud is among the leading contributors to the longwave term in large part because of its abundance, occurring roughly four times as often as any other cloud type (Figure 9c). The longwave covariances for the High & Mid and Deep clouds are high compared to the other categories, and they are abundant enough to have an impact on the overall longwave term (Figure 9a). Low, Mid, and Low & Mid clouds have a small mean longwave covariance and also a small total fraction, making their contribution to the overall longwave term negligible. Despite having the third largest longwave covariance, the High & Low cloud type has one of the smallest cloud fractions, making its overall contribution also very small.

There is a significant decrease in the contributions of High and High & Mid clouds to the longwave term as SST increases (Figure 9a). Figure 9b shows that the $LW'_n \times \widehat{h}'_n$ covariance remains similar for these cloud types across all SSTs, yet the fraction of these clouds decreases (Figure 9c). This suggests the sensitivity of the High and High & Mid cloud's longwave contribution to aggregation is predominantly due to the sensitivity of their abundance to SST. This decrease in anvil cloud fraction with SST is consistent with the stability iris mechanism described by Bony et al. (2016), who describe the reduction in anvil cloud as a consequence of increased anvil stability and decreased convective outflow with increasing SST.

The absolute longwave heating rates decrease with SST for all cloud types (not shown) because the longwave radiation out of the atmosphere (outgoing longwave radiation plus downwelling surface radiation) increases with SST more than the increase in upwelling surface radiation into the atmosphere. However, the non-normalized longwave heating anomalies tend to increase with SST. This is mainly because the fraction of high-topped cloud (with high longwave heating anomalies) is halved from the 295 K to the 305 K simulations (Figure 9c). This lowers the domain mean longwave heating, which increases the longwave anomaly of each category with SST and brings the domain-mean longwave

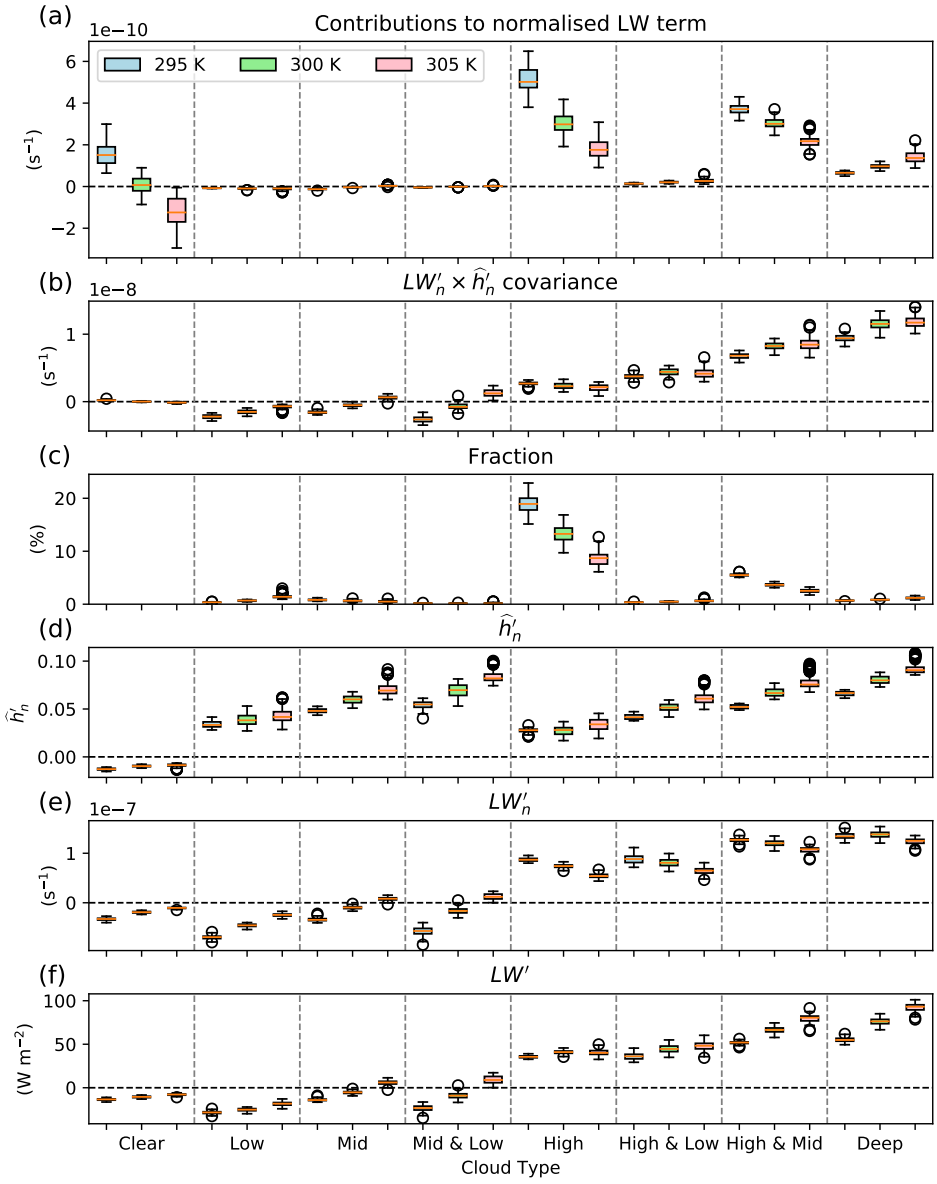

Figure 9. (a) Contribution to longwave term in equation (4) (b) normalized longwave × FMSE covariance, (c) cloud fraction (d) $\widehat{h}_n$ anomaly, (e) normalized longwave heating anomaly, and (f) longwave heating anomaly. Clear fractions are 73, 80 and 85% on average in order of increasing SST (not shown). Each data point represents the instantaneous domain-mean of the category. Orange lines indicate the median. Boxes represent the upper and lower quartiles, with the whiskers showing the range of the data. This is the range of data points that are within 1.5 times the interquartile range above and below the upper and lower quartile. Outliers above and below the whiskers (circles) are any data point that is outside this range. Boxes for each category are in order of SST increasing to the right. Data are from the final 20 days of the *LARGE* domains.

heating closer to that of the Clear regions. Once the longwave anomalies are normalized however, we see there is a slight decrease with SST for the significant cloud types as the difference between $\widehat{h}_{max}$ and $\widehat{h}_{min}$ increases. The decrease in the normalized longwave anomalies, along with the slight increase in $\widehat{h}'_n$ with SST, results in the $LW'_n \times \widehat{h}'_n$ covariance for the most abundant cloud types remaining approximately constant with SST.

4.2 Longwave Interactions within the Clear Regions

Figure 9a shows the contributions of the Clear regions to the longwave term decrease and become negative with SST. The reason for this is not immediately apparent, with the mean $LW'_n \times \widehat{h}'_n$ covariance becoming negative, despite both the mean LW'_n and mean $\widehat{h}'_n$ remaining negative (which would usually produce a mean positive covariance). This indicates that there must be a significant proportion of the Clear regions with large negative covariance which is able to reduce the overall contribution to the longwave term with increasing SST.

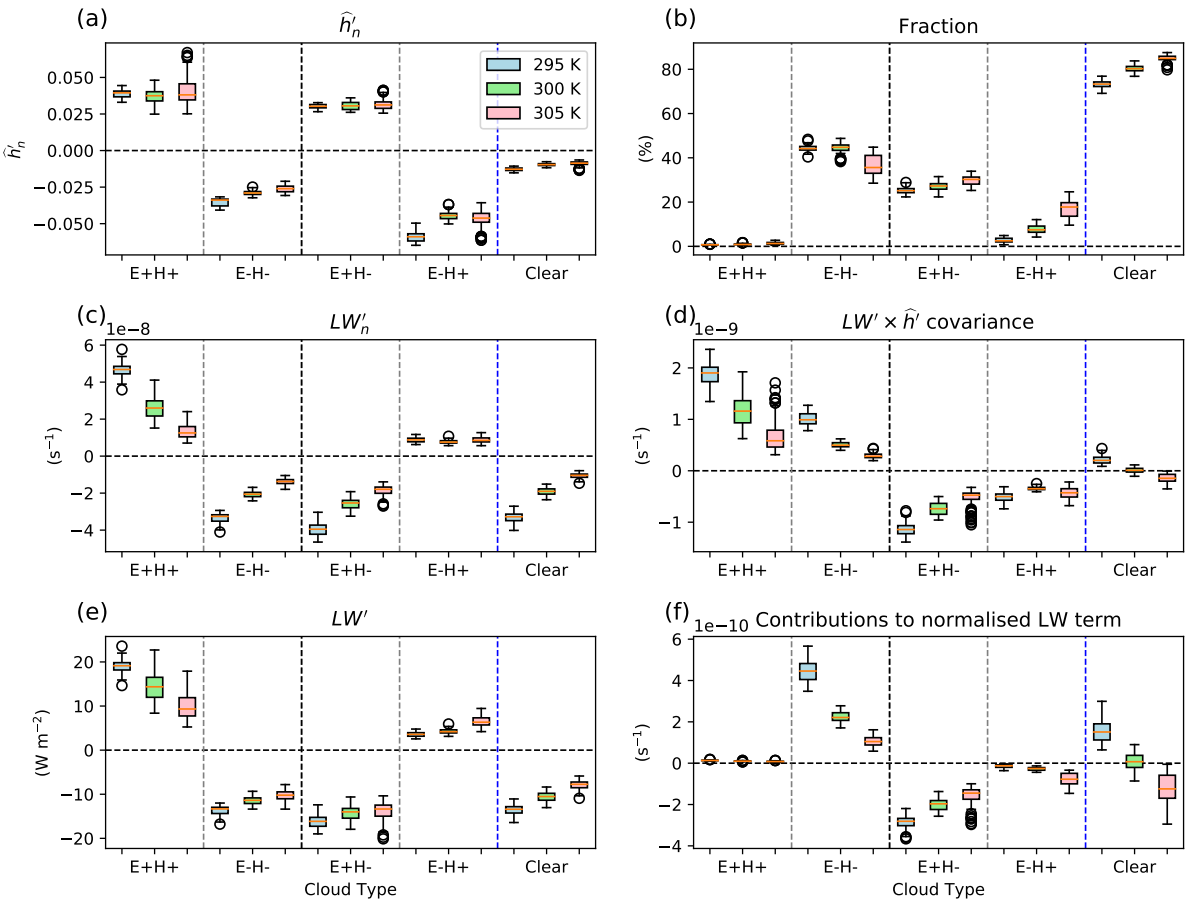

Figure 10. Instantaneous domain means of (a) $\widehat{h}_n$ anomalies, (b) cloud fraction (c) normalized longwave heating anomaly, (d) normalized longwave-FMSE covariance, (e) longwave heating anomaly, and (f) contribution to the normalized longwave term. Data from the final 20 days of the *LARGE* simulations.

We consider four types of Clear regions at play here whose significance changes with SST. There are the regions with both positive $\widehat{h}'$ and LW' (E+H+), regions with both negative $\widehat{h}'$ and LW' (E-H-), positive $\widehat{h}'$ and negative LW' (E+H-) and finally, negative $\widehat{h}'$ and positive LW' (E-H+). The Clear covariance quadrant map in Figure 6e shows

that E+H+ regions are rare and are found in the highest $\widehat{h}'$ areas, with a portion of these regions perhaps occurring as an artifact of the condensed water content used to define clouds. A lot of these E+H+ columns may indeed have enough high-altitude condensed water to produce a positive longwave heating anomaly. E+H- regions are typically found surrounding the cloud clusters, with E-H- occupying the majority of the dry regions. E-H+ occur only within the very driest areas. The E+H+ and E-H- regions both have a positive $LW' \times \widehat{h}'$ covariance whereas the E-H+ and E+H- regions have a negative covariance. By calculating the domain fraction of these regions, as well as their mean LW'_n and $\widehat{h}'_n$ and their mean $LW'_n \times \widehat{h}'_n$ covariance, we can see how their influences on the longwave term changes with SST. These calculations are shown in Figure 10.

There is a shift in dominance from the positive covariance regions to the negative covariance regions as the SST increases. For all SSTs, the E+H+ regions only occupy around 1% of the domain, making their overall contribution to the longwave term negligible. At 295 K, there are two significant Clear regimes; E-H-, occupying 44% of the domain and E+H-, occupying 25%. They have similar but opposite LW'_n *times* $\widehat{h}'_n$ covariances, so the Clear region's contribution to the longwave term is dominated by the E-H- regions based on their abundance. This results in a positive contribution of the Clear regions to the longwave term.

As SST increases, the LW' of the Clear regions as a whole becomes significantly less negative (Figure 10e). This is likely due to the approximate halving in the abundance of High and High & Mid clouds, which both have a strong positive longwave heating anomaly. This then reduces the domain-mean longwave heating rate, making the longwave anomaly of the Clear regions less negative. After normalizing the longwave anomalies, the SST sensitivity is even more notable (Figure 10c). The contribution of the E-H- regions falls rapidly as the $LW'_n \times \widehat{h}'_n$ covariance decreases. At the same time, the E-H+ regions become far more abundant, also helping to decrease the Clear region's contribution to the longwave term. This feature was also noted by Wing and Emanuel (2014) and Emanuel et al. (2014), who explain that extremely dry columns with little low-level moisture are unable to effectively emit radiation, resulting in anomalous warming.

The magnitude of $\widehat{h}'$ are largest for the two regimes with positive LW'. This is because the relationship between $\widehat{h}$ and longwave heating within the Clear regions is not linear; the strongest longwave cooling occurs roughly where $\widehat{h}'$ is zero for all SSTs. This can be understood by breaking the net atmospheric longwave heating down into the individual longwave fluxes into the atmosphere minus the outward fluxes. Each of these terms are plotted against $\widehat{h}'_n$ in Figure 11b.

Water vapor is a strong absorber and emitter of longwave radiation, so the higher the water vapor content, the higher the opacity of the atmosphere to longwave radiation. Having water vapor at higher altitudes will raise the effective level of emission to a cooler altitude, and decrease the OLR. Similarly, higher humidity at lower altitude will decrease the effective downward emission level to a warmer altitude, therefore increasing the downwelling emissions to the surface. The effective upward emission level is defined as the altitude at which the temperature is equal to the OLR divided by σT^4, where σ is the Stefan-Boltzmann constant. Similarly, the effective downward emission level is the altitude at which the temperature is equal to the downwelling longwave radiation divided by σT^4. Figure 11a shows that, starting from the lowest $\widehat{h}_n$ values, the rate of change of specific humidity with $\widehat{h}_n$ decreases at higher altitudes above the boundary layer. This means the change in effective OLR emission height with $\widehat{h}_n$ initially increases at a slower rate than the decrease in the effective downwelling emission height. This results in a decreasing net longwave heating rate as we increase $\widehat{h}_n$ towards a zero $\widehat{h}'_n$. This means that positive longwave anomalies are likely to occur at extremely negative $\widehat{h}'_n$ regions, which leads to the E-H+ regions having a significant $LW'_n \times \widehat{h}'_n$ covariance despite having the lowest LW'_n.

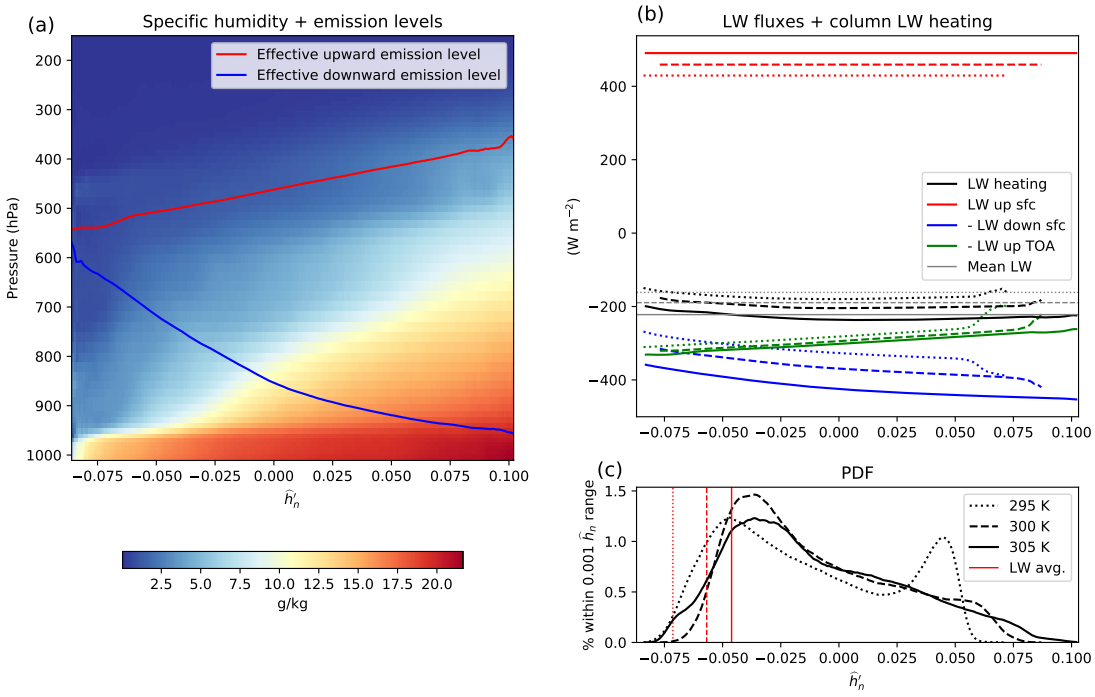

Figure 11. (a) Specific humidity profiles against $\widehat{h}_n$ anomaly for *LARGE* domain with 305 K SST for the final 20 days. Effective level of outgoing TOA longwave emission shown in red, effective level of longwave emission into the surface shown in blue. (b) All longwave fluxes into, and out of the atmosphere plotted against $\widehat{h}_n$ anomaly. 295 K: dotted, 300 K dashed, 305 K: solid. The fluxes out of the atmosphere are plotted with positive direction into the atmosphere so that the three fluxes add together to equal the net longwave heating. Horizontal grey lines indicate the domain-mean longwave column heating. (c) Percentage of Clear grid points within a given 0.001 $\widehat{h}'_n$ range. Clear regions to the left of the red line have a positive longwave anomaly on average.

As $\widehat{h}_n$ increases from a zero $\widehat{h}'_n$, the effective downward emission level begins to decrease at a slower rate than the OLR emission level increases. This could be because the low levels become so humid that it becomes increasingly difficult to decrease the altitude of the downward emission level. This means that the net longwave heating rates begin to increase with $\widehat{h}_n$ above a zero $\widehat{h}'_n$. We do not have an explanation as to why the longwave heating minima happens to occur around a zero $\widehat{h}'_n$.

With the mean longwave heating rates skewed more toward the clear longwave heating rates with increasing SST, there is a greater quantity of clear regions with positive LW'. This can be seen in Figure 11c, noting the tails of the $\widehat{h}_n$ distributions extend more into the regions with positive longwave heating anomalies as SST increases.

4.3 Shortwave Interactions

Figure 12 shows that shortwave feedbacks in the Clear regions contribute the most to the shortwave term once the domain is aggregated. However, this may be an artifact of the large fraction of the Clear regions. It can be seen from Figure 6b and d that there is a very strong relationship between both FMSE and shortwave anomalies. This is because variations of FMSE are dominated by changes in water vapor, which is an excellent absorber of shortwave radiation. This results in the shortwave-FMSE covariance being positive at almost every location (e.g. Arnold & Putman, 2018).

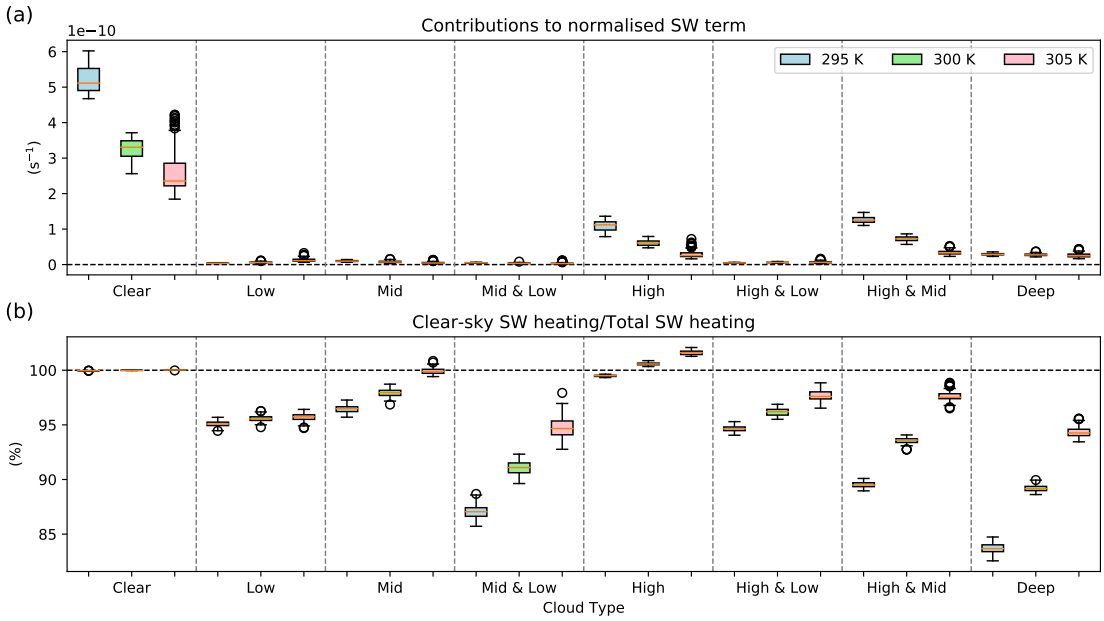

Figure 12. Instantaneous domain-means of (a) contribution to the normalized shortwave term in equation (4), (b) Clear-sky heating divided by total shortwave heating rate. Data from the final 20 days of the *LARGE* simulations.

A large portion of the cloud contribution to the shortwave term is due to the amount of water vapor in the column. The contribution of water vapor to the column shortwave heating rate can be quantified by calculating the clear-sky heating rates and dividing by the total heating rates for each category as shown in Figure 12b. The total shortwave heating rates can almost entirely be explained by the column WVP, particularly at higher temperatures where the quantity of water vapor is higher, making the condensed water content less significant at higher temperatures. The clear-sky component of the total shortwave heating rate is lowest for clouds with the highest CWP since there is a higher fraction of the heating rate due to condensed water. The clear-sky heating rate is sometimes higher than the all-sky heating rate for the high clouds since the cloud reflects the radiation that would otherwise have been absorbed by the low-level water vapor.

The contribution of the shortwave term to aggregation is highly sensitive to SST, becoming less important as SST increases. This is because the range of SW_n' decreases with increasing SST, whereas the range of $\widehat{h}_n$ remains similar. This results in the domain-mean normalized shortwave-FMSE covariance, and therefore, the shortwave term, decreasing with SST (analysis not shown). The range of column WVP across the domain increases exponentially with SST, whereas the relationship between column shortwave heating with WVP is logarithmic (Vaquero-Martínez et al., 2018). This results in the range of shortwave heating across the domain remaining similar. Once the shortwave heating anomalies are divided by $\widehat{h}_{max} - \widehat{h}_{min}$, SW_n' decreases with increasing SST.

5 Cloud Type Contributions throughout the Aggregation Process

So far, we have only discussed the radiative interactions within the already-aggregated *LARGE* domains. In this section, we look at the key radiative-convective interactions responsible for the development of aggregation.

As with the previous sections, the domain-mean longwave and shortwave heating rates and covariances are found for each category, as well as their domain fraction. From this, the mean longwave and shortwave contributions for each category can be found. Time

series of these variables as well as the mean $\widehat{h}'$ for each category are shown in Figure 13 for the *LARGE*, 300 K simulation.

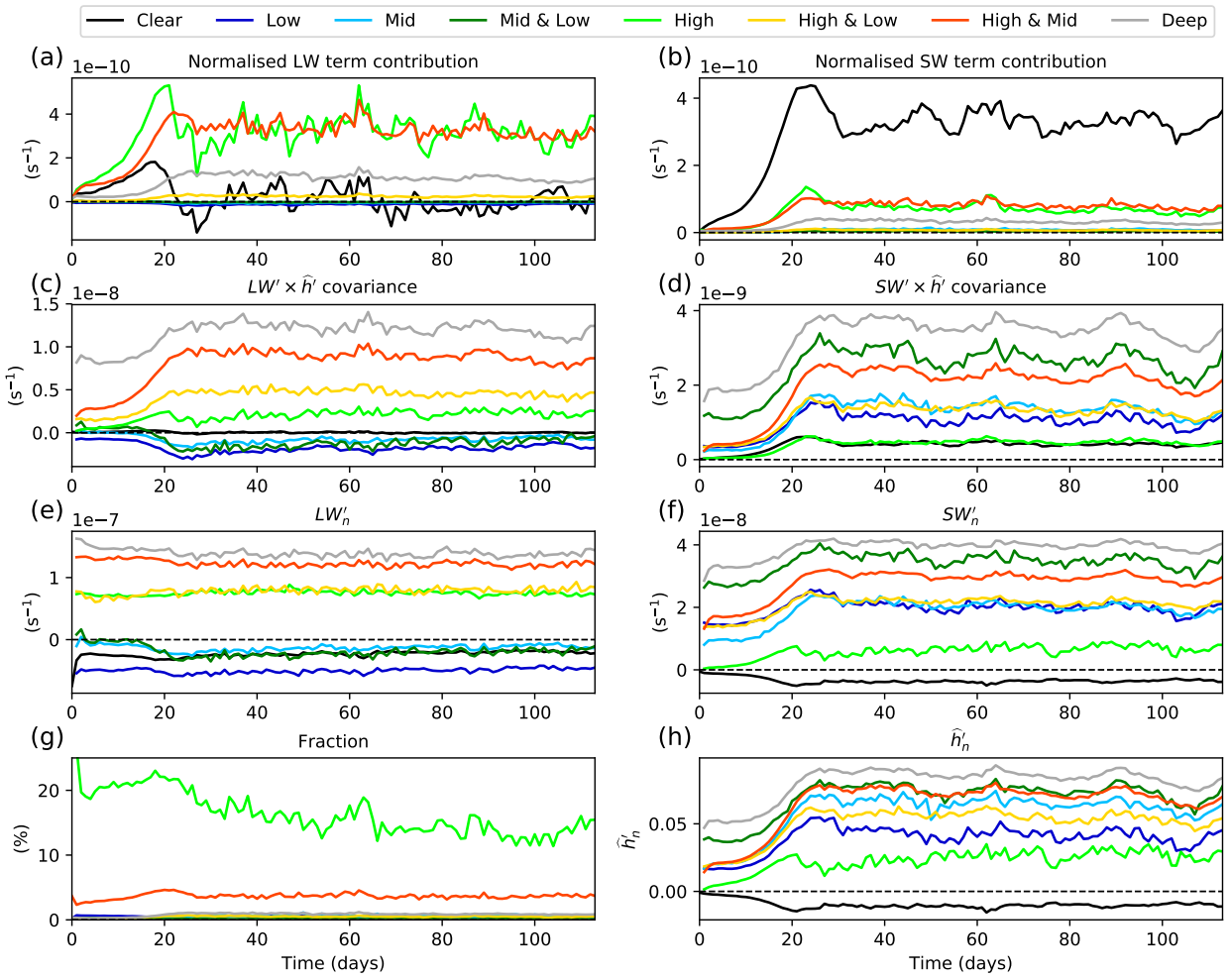

Figure 13. Time series of contributions to the (a) normalized longwave and (b) normalized shortwave term, (c) the normalized longwave, and (d) shortwave × FMSE covariances, normalized (e) longwave and (f) shortwave heating anomalies, (g) domain fraction (excluding Clear), and (h) $\widehat{h}_n$ anomaly of each cloud category. For the entirety of the *LARGE*, 300 K simulation. Each data point is a daily average.

Interactions between clouds and longwave radiation are the main drivers of aggregation at early times. This is also shown in Figure 5 (note that the sum of the contributions in Figure 13a and 13b equal the total radiative terms in Figure 5). Throughout the aggregation process, each category's contribution to both radiative terms increases rapidly. This is due to the positive feedback between radiative heating and $\widehat{h}$. Anomalous heating in anomalously high $\widehat{h}$ regions causes $\widehat{h}$ to increase. Higher $\widehat{h}$ regions are favorable for deep convection, resulting in more anomalous heating in both the longwave and shortwave. In anomalously low $\widehat{h}$ regions, deep convection is suppressed, resulting in enhanced radiative cooling, further decreasing the FMSE. These feedbacks are the dominant radiative processes that increase var($\widehat{h}$) in our simulations.

The effect of clouds on the shortwave term is sensitive to SST and the degree of aggregation. This is shown in the time series of the clear-sky component of the shortwave term shown in Figure 14. At early times, there is little variation in horizontal distribution of water vapor, so the shortwave absorption by clouds has a significant impact on the mean $SW'_n \times \widehat{h}'_n$ covariance. At these times, the shortwave absorption by condensed water accounts for between 30% and 50% of the shortwave term, with clouds having a larger impact at colder SSTs due to the decrease in tropospheric water vapor. As soon as dry and moist patches begin to develop, the horizontal variations in the shortwave absorption of water vapor dominate the shortwave term, accounting for 87% - 96% of the shortwave term as SST increases once the domains are aggregated.

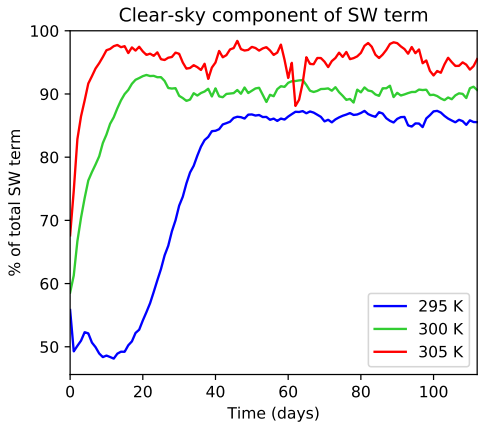

Figure 14. Time series of the daily-mean clear-sky component of the shortwave term, calculated as the domain-mean shortwave term divided by the domain-mean shortwave term using clear-sky heating.

It is the longwave interactions with high-topped cloud, as well as the shortwave interactions with water vapor, that are the key radiative interactions that act to increase var($\widehat{h}$), and hence drive aggregation. These results are sensitive to SST. As SST increases, the fraction of high-topped cloud decreases, resulting in a decrease of the longwave contribution to aggregation, proportional to the decrease of this cloud fraction change. The shortwave interactions become less significant for driving aggregation as SST increases. The clear-sky shortwave contribution is inversely proportional to the difference between $\widehat{h}_{max}$ and $\widehat{h}_{min}$, and the differential shortwave absorption between cloudy and clear regions decreases with SST as the atmosphere contains more water vapor. This results in the shortwave interactions being approximately three times more important in driving aggregation at 295 K compared to 305 K. Within this domain setup, low-level clouds have a negligible direct contribution to the radiative terms because of their low fraction and low radiative $\times \widehat{h}'$ covariances, although other studies have shown that the radiatively-driven circulations they generate may be significant to the aggregation process (Muller & Held, 2012).

LW'_n for each category remain approximately constant with time whereas SW'_n for each cloud category increase by around 5 W m^{-2} as aggregation increases. The average SW'_n for the Clear regions decreases by around 3 W m^{-2} as the convection aggregates. This is because the condensed water content in a column is the dominant factor in determining the longwave heating of that column, whereas the total water content of the column is the dominant factor in determining the column shortwave heating. As the convection becomes more aggregated, all cloud categories find themselves in moister environments, thereby increasing their shortwave anomalies.

At early stages of aggregation, the Clear regions have a large positive contribution to the longwave term. At this time, the Clear regions' longwave contribution is dominated by the E-H- and the E+H- regions due to their abundance (Figure 15). This is consistent across all SSTs (not shown). The positive longwave covariance E-H- regions have a larger contribution than the negative covariance E-H+ regions at early stages, however the $LW'_n \times \widehat{h}'_n$ covariance of the E-H- regions stops increasing earlier than the E-H+ regions. At later stages of aggregation, there is also a sharp increase in abundance of the E-H+ regions particularly at higher SSTs (not shown). As the negative covari-

ance regions continue to increase, the Clear regions' longwave contribution then begins to decrease and can become negative.

6 Comparison of Convection within High-Resolution Simulations

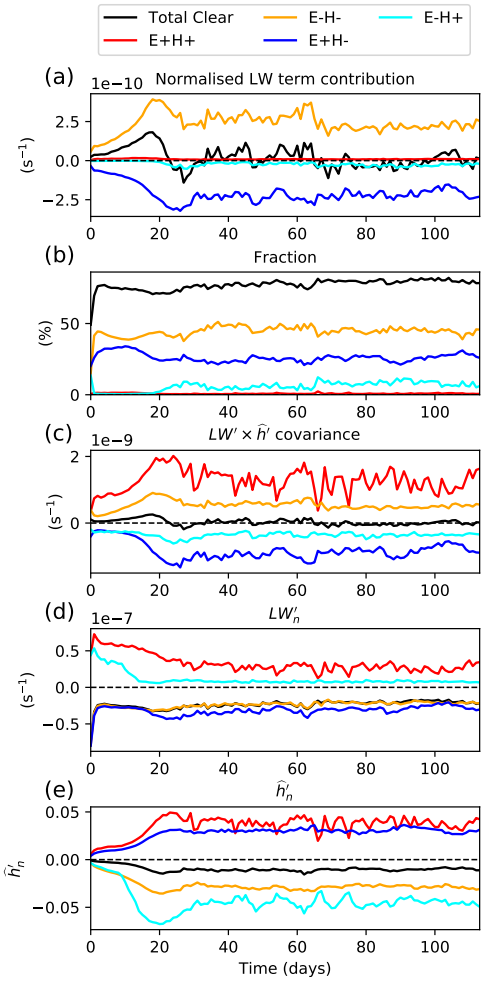

Figure 15. Time series of (a) contributions to the normalized longwave term, (b) domain fraction, (c) mean normalized longwave × FMSE covariances, (d) normalized longwave anomaly, and (e) $\widehat{h}_n$ anomaly of each Clear category. For entire period of the *LARGE*, 300 K simulation. Each data point is a daily average.

In the previous sections, only radiative interactions within *LARGE* domain simulations have been analyzed. In addition to these, we have also simulated the three-SST RCEMIP cases in three new model configurations on a smaller (100 km x 100 km) horizontal domains to investigate how the above SST-dependent features of RCE convection and its radiative interactions are affected by changes to model grid spacing and the treatment of subgrid condensation. Subgrid condensation occurs when the grid point's relative humidity reaches the RHcrit value. With this value being set to 0.99, it is too high to yield a reasonable cloud field and is the reason for the considerable lack of low cloud compared to similar models compared in RCEMIP (Wing et al., 2020).

With the length scale of the aggregated features in the *LARGE* domain being many times larger than the dimensions of our smaller simulations, we are not able to quantify how these changes in resolution and RHcrit explicitly affect aggregation. However, we are able to see how the radiative properties of the clouds are affected. We can then imply how these changes in the radiative properties of cloud may impact aggregation in larger-scale simulations.

Since the aggregation states between the *LARGE* and the *SMALL* simulations are inevitably very different, we try to analyze times where domain size and aggregation state do not have a significant impact on the cloud structures. With the convection aggregating rapidly within the *LARGE* 300 and 305 K simulations, we have chosen to only compare days two to six of the *LARGE* domains against days two onwards of the smaller domains.

Profiles of cloud fraction reveal that both grid spacing and RHcrit strongly influence the vertical structure of clouds across the domain (Figure 16). This figure shows only the 300 K simulations, although the same changes are seen at the other SSTs, only shifted in altitude as the tropospheric depth is larger for higher SSTs. As the grid spacing is reduced, there is a sharp increase in the quantity of low and mid-level cloud, with

this increase being most apparent when looking at the *SMALL_HI* simulation. Low-level clouds generally have smaller length scales so cannot be resolved in coarser grid spacings due to the unrealistically high RHcrit value used. Our original RHcrit value becomes more suitable at lower grid spacings, effectively representing these small-scale clouds more realistically. There is also a decrease in altitude of high-level clouds with decreasing grid spacing, with a corresponding increase in high-cloud temperature. This contributes to an increase in OLR for high-topped clouds, reducing their anomalous longwave heating rates.

As the RHcrit is decreased to that used in the Met Office UKV model, the overall cloud amount increases. This comes from an increase of more than an order of magnitude in low-level cloud and also a significant increase in mid-level cloud. The upper-level cloud amounts remain largely unchanged. Fractions of the High, and High & Mid cloud types are greatly reduced due to the increase in low and mid-level clouds, in turn increasing the quantities of the High & Low and Deep cloud types.

Comparisons of cloud type fraction, normalized longwave and shortwave heating anomalies, and CWP for each cloud category, SST and domain configuration are shown in Figure 17. From this, the resolution dependence of the radiative terms for self-aggregation may be inferred.

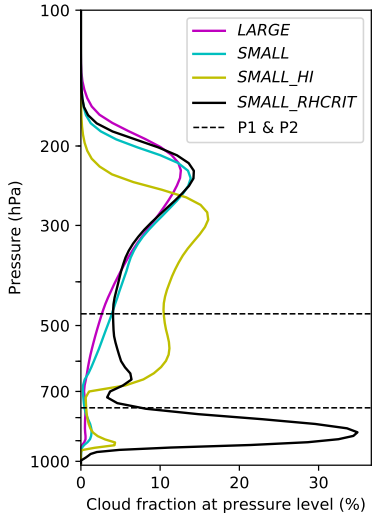

Figure 16. Temporally-averaged cloud fractions for each domain setup at 300 K. *LARGE* domain averages are for days 2-6, whereas each of the smaller domains are averaged from day 2 onward. Horizontal dashed lines represent the low and high cloud thresholds (P1 and P2).

There is a significant decrease in the absolute longwave heating rates of high-topped clouds with both decreasing grid spacing and decreasing RHcrit (not shown). This is mainly due to an increase in OLR rather than an increase in the downwelling longwave radiation which remains approximately constant for these categories with grid spacing (not shown). This increase in OLR may be mostly explained by the change in cloud top height with as well as the decrease of CWP. There is an associated increase in cloud top temperature with decreasing altitude, which increases OLR. The cloud top height is likely reduced due to the increased updraft mixing of the higher-resolution simulations, decreasing updraft buoyancy, and thus the maximum altitude of the plume. The CWP decreases for the majority of cloud types as the critical condensation humidity is reached more widely, i.e. by decreasing RHcrit or decreasing the grid spacing. Since water vapor is more readily condensed, the clouds that do form are more widespread and less concentrated. A decreasing CWP of these high-topped clouds decreases their opacity to longwave radiation, decreasing the effective level of emission. This also increases OLR, helping to lower their longwave heating rates.

The longwave heating rates of the remaining cloud categories without high-level cloud remain similar with grid spacing and RHcrit. As shown in Figure 7a, the longwave heating rates of these cloud types are less dependent on CWP in the *LARGE* simulations. The combined fractions of the lower longwave heating rate categories (Clear, Low, Mid and Mid & Low categories) remain similar with resolution and RHcrit, and remain far more abundant than the high-topped cloud categories with relatively high longwave heating rate categories. This reduces the spread of longwave heating rates across the domain, decreasing the magnitude of the longwave anoma-

lies for the majority of categories. This may decrease the $LW'_n \times \widehat{h}'_n$ covariance in moist regions and may significantly reduce the longwave term. An increase in Low and Mid & Low cloud may also significantly reduce the longwave term since they have strong negative heating rates and are mainly found in positive FMSE anomaly regions so have a negative $LW'_n \times \widehat{h}'_n$ covariance on average.

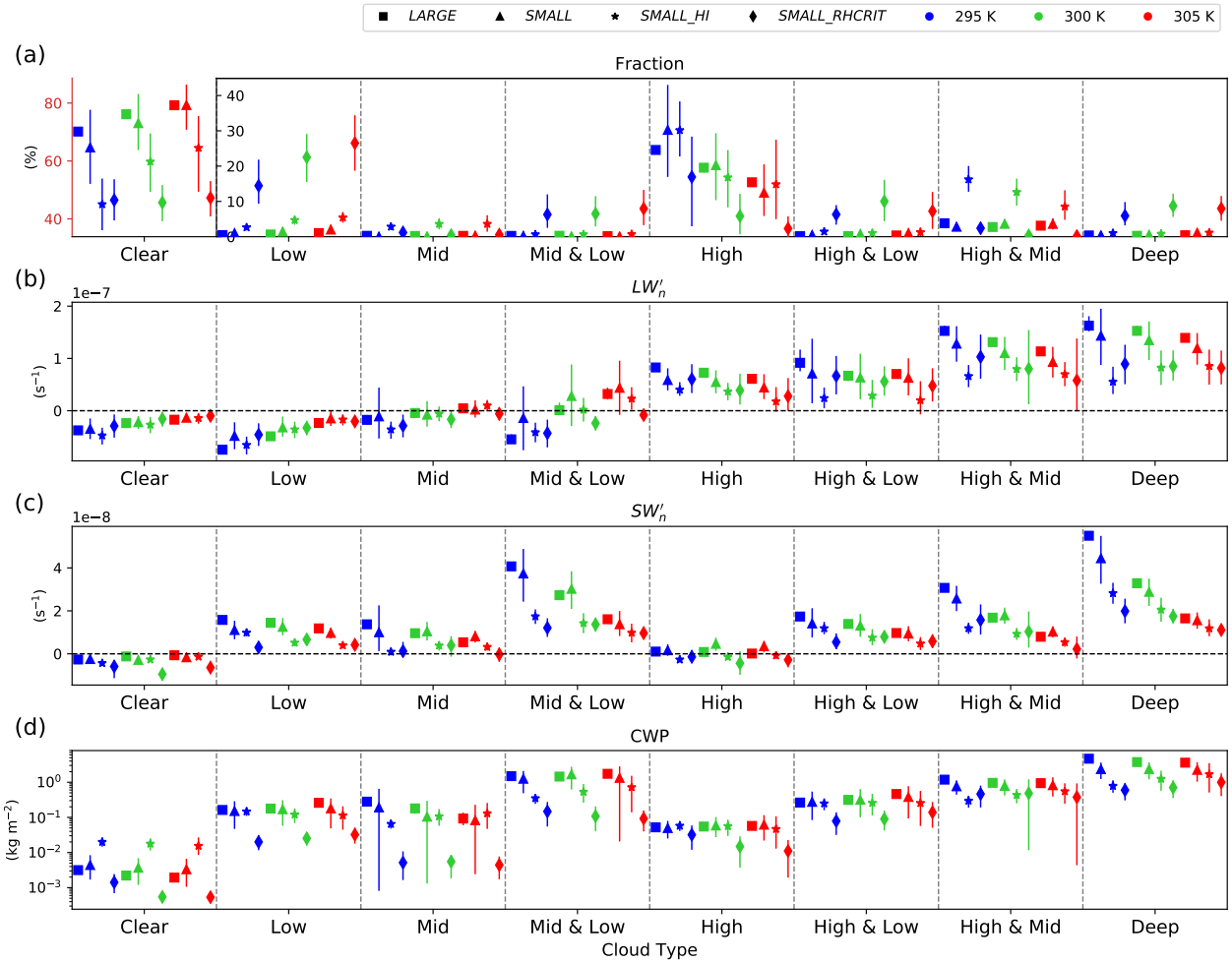

Figure 17. Instantaneous domain-means of (a) domain fraction, (b) normalized longwave heating anomaly, (c) normalized shortwave heating anomaly, and (d) condensed water path, for each cloud category within all domain setups and SSTs. *LARGE* domain averages are for days 2-6, whereas the *SMALL* and *SMALL_HI* averages are for days 2-54. Note that the fraction of the Clear regions (top-left panel) are on a separate axis to the remaining cloud types. Vertical bars represent the range of the 10th to 90th percentile.

As grid spacing is reduced, we find an increase in mid-level cloud, resulting in a decrease in the High category fraction and an increase in High & Mid, which typically have higher LW'_n. However, the mean LW'_n of all clouds in the domain is reduced as grid spacing is reduced. With clouds tending to occur in high-FMSE regions, it is argued that the domain-mean longwave term would be reduced. A similar result is seen in the reduced RHcrit simulation, with the increased low cloud resulting in fewer High and High & Mid columns, and more Deep, which again typically has higher LW'_n. However, the mean LW'_n

of all the clouds is again reduced, and is mainly a result of the increased Low cloud fraction with negative LW'_n.

Cloud-radiation trends with SST in the *LARGE* domain are largely consistent across the grid spacings tested. The total high-topped cloud fraction decreases with SST by a similar amount, as does the decrease in LW'_n for these clouds, meaning trends in the radiative terms to aggregation with SST would likely be similar. This is mainly true for the reduced RHcrit simulations, however with Low cloud approximately doubling from 295 K to 305 K, the magnitude of the longwave term would decrease faster with SST than our original RHcrit simulations.

The shortwave heating rates of columns with cloud are generally significantly reduced with decreasing grid spacing and RHcrit and could be due to the decrease in the CWP with less shortwave radiation being absorbed by condensed water. This may slightly reduce the magnitude of the shortwave term at early times, although the other terms in the FMSE variance budget are more important at these early stages of aggregation. The shortwave heating rates depend more on the overall distribution of water vapor which is in turn affected by the degree of aggregation. So, we would have to understand how sensitive the other terms are to resolution and RHcrit before determining the sensitivity of the shortwave term.

When analyzing the *LARGE* domain, we found that longwave interactions with high-topped clouds is the main driver of aggregation, with their overall impact reducing with SST as anvil cloud fraction reduces. As the grid spacing and RHcrit are reduced for smaller, less-aggregated domains, we still find that high-topped clouds reduce in abundance, indicating that smaller high-topped cloud fraction with increased SST is a consistent trend regardless of these parameters. We also found that Clear regions have a significant positive contribution to aggregation at cooler SSTs, with this contribution decreasing with SST and becoming negative. The longwave heating rates of high-topped clouds are lower in the reduced RHcrit simulations, in turn lowering the domain-mean longwave heating. This makes the longwave heating anomalies of the Clear regions less negative, further lowering the Clear contributions to the longwave term. This downward trend with SST remains consistent across all of our simulations.

These results can be used to infer how aggregation may be affected in large domains with smaller grid spacings and at the lower RHcrit. By decreasing the grid spacing, there is an associated decrease in the anomalous longwave heating of high-topped clouds, as a result of a decreased cloud-top height and decreased CWP. This also increases the mean radiative cooling of the entire domain, making the clear regions' longwave cooling less anomalous. With reduced anomalous longwave heating in high-FMSE regions, and reduced anomalous cooling in low-FMSE regions, the $LW'_n \times \widehat{h}'_n$ covariance will be reduced on average across the domain, slowing the rate of aggregation. The shortwave term is largely dependent on the degree of aggregation. However at early times, the shortwave absorption by clouds has a significant contribution to the aggregation. With CWP decreasing as the grid spacing is reduced, there will be lower differential shortwave absorption between typically higher-FMSE cloudy regions and lower-FMSE clear regions, reducing the $SW'_n \times \widehat{h}'_n$ covariance, further reducing the rate of aggregation.

Similar conclusions can be made from the decreased RHcrit simulations. Reduced CWP of high-topped clouds reduces their longwave heating rates. Together with the increase in Low cloud, the longwave heating rates in high-FMSE regions will be significantly reduced. Again, this has the side effect of reducing the anomalous longwave cooling of clear regions. Overall, the $LW'_n \times \widehat{h}'_n$ covariance across the domain would decrease, slowing the rate of aggregation. The reduced CWP of clouds again reduces the differential shortwave absorption between cloudy and Clear regions, lowering the $SW'_n \times \widehat{h}'_n$ covariance, slowing the rate of aggregation.

7 Conclusions

In this study, we quantify the dominant direct radiative interactions that drive and maintain aggregation within large channel domain simulations of radiative-convective equilibrium (RCE) of the Met Office Unified Model version 11.0 following the RCEMIP protocol (Wing et al., 2018). We have assessed the sensitivity of these interactions to sea surface temperature (SST) by comparing simulations with fixed SSTs of 295, 300 and 305 K using the normalized column-integrated FMSE ($\widehat{h}_n$) variance budget as our framework for studying self-aggregation. We particularly focus on the role of cloud-radiative interactions, assigning one of eight different cloud types to each grid column. We also investigate how the key radiative interactions are affected by both grid spacing the critical condensation relative humidity parameter (RHcrit) using smaller (100 km $\times$ 100 km) domains.

The instantaneous horizontal variance of normalized vertically-integrated FMSE, var($\widehat{h}_n$), is a consistent aggregation metric across all SSTs, with values below 10^{-4} corresponding to randomly scattered convection, and values greater than 10^{-3} corresponding to highly aggregated convection. The var($\widehat{h}_n$) budget equation (equation 4) states how the rate of change of var($\widehat{h}_n$), and hence the rate of change of aggregation, is driven by feedbacks between anomalies in $\widehat{h}_n$ and anomalies in normalized column-integrated longwave heating, shortwave heating, surface fluxes, and advection of $\widehat{h}_n$. This study focuses on the two radiative terms of this equation (longwave and shortwave), which show that regions with a positive covariance between the normalized radiative anomalies (LW'_n and SW'_n) and $\widehat{h}'_n$ help to increase aggregation.

For all SSTs within our *LARGE* domains, the longwave radiative term in equation (4) is the main driver in increasing the horizontal variance of $\widehat{h}_n$ at early times, hence increasing aggregation, and both the longwave and shortwave terms help maintain aggregation. Despite each of these simulations reaching a similar state of aggregation (by the var($\widehat{h}_n$) metric), the magnitude of the longwave and shortwave terms decrease with SST both in the aggregating, and aggregated phases. The decrease in the radiative terms are balanced by a decrease in magnitude of the mainly negative surface enthalpy flux and advection feedback terms. In our simulations, the sensitivity of the advection-FMSE feedback to SST is the dominant factor in determining how the rate of change of aggregation at early times changes with SST.

High-topped clouds produce the largest positive column-integrated longwave heating anomalies, whereas low level clouds produce negative anomalies, with the magnitude of these anomalies generally increasing within the typical condensed water path (CWP) range that they are found. The mean $\widehat{h}'_n$ for each cloud type is positive, therefore clouds with a positive radiative anomaly have a positive radiative $\times$ $\widehat{h}'_n$ feedback and vice versa. The average $LW'_n \times \widehat{h}'_n$ covariance for each of the key cloud types remains similar with SST, meaning an individual cloud's longwave contribution to self-aggregation remains similar. The SST dependence of the total longwave contribution is due to the sensitivity of cloud fraction to SST. High-topped clouds have large, positive anomalies in longwave heating and FMSE, and they are the most abundant types of cloud so they contribute the most to the longwave term. As SST increases, from 295 K to 305 K, their abundance is approximately halved, and so too is their longwave contribution to aggregation.

Longwave interactions within the clear regions can have a large impact on the total longwave term, although their contributions to the longwave term are highly sensitive to SST and aggregation. The longwave contribution of the clear regions is large and positive during early stages of aggregation and decreases with aggregation and SST, becoming strongly negative during the fully aggregated stage of the high SST simulation. The clear regions' longwave contribution turns negative when the dry patches become amplified and extremely dry. This is a feature also identified by Wing and Emanuel (2014)

and Emanuel et al. (2014) and can be explained by the reduced ability of extremely dry regions to effectively emit radiation, resulting in anomalous heating. We show that the typically negative longwave heating anomalies in the clear regions become less negative with SST as a result of the domain-mean longwave heating becoming increasingly negative. This is due to the reduction of high clouds which have a strong anomalous longwave heating effect, increasing the domain-mean radiative cooling. The mean covariance between the longwave heating and FMSE anomalies becomes negative, meaning the clear regions have a negative contribution to aggregation at high SSTs.

Shortwave anomalies are approximately 6 times smaller in magnitude than longwave anomalies, however the domain-mean shortwave term is similar in magnitude to the longwave term once the convection is aggregated. This is because the $SW'_n \times \widehat{h}'_n$ covariance is positive at almost all times and locations, with positive FMSE anomalies yielding positive anomalous shortwave heating rates mainly due to the shortwave absorption by water vapor. Shortwave anomalies are positive on average for all cloud types at all CWPs and is likely due to them mainly occurring in anomalously humid environments, allowing absorption of shortwave radiation by water vapor to dominate the shortwave heating rates.

The magnitude of the mean shortwave-FMSE feedbacks are heavily dependent on the horizontal spread of water vapor and therefore the state of aggregation. At very early times, when the water vapor path field is approximately uniform, the role of shortwave feedbacks are outweighed by the role of longwave, surface flux, and advective feedbacks with FMSE. The contribution of clouds to the shortwave term also depends on the level of aggregation. At very early times, the additional shortwave absorption of condensed water results in clouds contributing to around 50% of the shortwave term at 295 K and 30% at the 305 K SST. As soon as distinct moist and dry patches begin to develop, the differential absorption of shortwave radiation by water vapor rapidly increases the clear-sky component of the shortwave term to 87%-96% of the total shortwave term (from 295 K - 305 K). The shortwave term's dependence on grid spacing and RHcrit depends of the sensitivity of aggregation itself to these factors.

Model grid spacing affects the radiative properties of clouds in a number of ways. We find that decreasing grid spacing reduces the mean CWP of clouds, decreases the cloud top height of high clouds, and produces more low and mid-level cloud. The overall effect of these changes to the cloud properties is a reduced mean longwave heating anomaly of high-FMSE cloudy regions. This would decrease the domain mean covariance between longwave heating and FMSE anomalies, slowing the rate of aggregation for hypothetical high-resolution large-domain simulations. Sensitivities with SST that we find in the large domain remain similar with grid spacing, meaning the magnitude of the decrease in the longwave term with SST would likely remain similar with reduced grid spacing in larger simulations.

When lowering the RHcrit parameter to that used in the Met Office UKV model, we find significant changes in the distribution, structure, and radiative properties of cloud. Firstly the low level cloud fraction increases from $\sim 1\%$ in the *SMALL* domain to between 15% and 30% within the *SMALL_RHCRIT* simulations. There is also an increase in mid-level cloud, and the high-level cloud remains similar. However, as the cloud fraction increases, the mean cloud CWP decreases, altering the associated longwave heating rates. With high-level clouds maintaining a similar fraction but having a decreased CWP, their longwave heating anomalies fall, significantly reducing their contribution to the longwave term. With the increase in low clouds, with their typically negative longwave-FMSE covariance, the longwave term is further reduced, so these combined effects would likely lead to a slower rate of aggregation if this RHcrit is used in a large domain. With the sharp increase in low cloud with SST, the longwave term would likely decrease at a faster rate than the decrease seen in our large simulations, suggesting aggregation could be slowed at higher SSTs using this RHcrit value in large-domain simulations.

There is much variability in the degrees of aggregation and within numerical models of RCE, which has important consequences for weather and climate (Wing et al., 2020). With radiative interactions between cloud and moisture being the dominant drivers and maintainers of aggregation in our models, understanding how these interactions vary between other RCE models may go some way in explaining the differences in self-aggregation and this is a focus of our ongoing work. By building on the analysis technique of Wing and Emanuel (2014), this paper provides a framework by which a comparison of cloud-radiative interactions and their contributions to self-aggregation between models and SSTs can be achieved. This technique is suitable for all models with a fixed SST. Its use for model/reanalysis studies with a varying SST would require the normalization of $\widehat{h}$ to vary in space and time.

Acknowledgments

This work was supported by the Natural Environment Research Council SCENARIO DTP (NE/L002566/1). The simulations of the UM have been produced by Todd Jones, supported by the Natural Environment Research Council (NERC) under the joint NERC/Met Office ParaCon program's Circle-A project (NE/N013735/1), as well as the ParaCon Phase 2 project: Understanding and Representing Atmospheric Convection across Scales (NE/T003871/1). The simulations have been conducted using Monsoon2, a High Performance Computing facility funded by the Met Office and NERC, the NEXCS High Performance Computing facility funded by NERC and delivered by the Met Office, and JASMIN, the UK collaborative data analysis facility. We thank the German Climate Computing Center (DKRZ) for hosting the standardized RCEMIP data for the *LARGE* and *SMALL* simulations, which is publicly available at http://hdl.handle.net/21.14101/d4beee8e-6996-453e-bbd1-ff53b6874c0e. All data used for plotting each figure, as well as the original python scripts are available on Zenodo at: https://doi.org/10.5281/zenodo.4586097. We also acknowledge Mike Whitall (UK Met office) and Steve Woolnough (University of Reading) for their valuable insights and suggestions.

References

Arakawa, A., & Schubert, W. H. (1974). Interaction of a Cumulus Cloud Ensemble with the Large-Scale Environment, Part 1. *Journal of the Atmospheric Sciences*, *34*, 674–701. doi: 10.1175/1520-0469(1974)031⟨0674:IOACCE⟩2.0.CO;2

Arnold, N. P., & Putman, W. M. (2018). Nonrotating Convective Self-Aggregation in a Limited Area AGCM. *Journal of Advances in Modeling Earth Systems*, *10*(4), 1029–1046. doi: 10.1002/2017MS001218

Arnold, N. P., & Randall, D. A. (2015). Global-scale convective aggregation: Implications for the Madden-Julian Oscillation. *Journal of Advances in Modeling Earth Systems*, *7*, 1499–1518. doi: 10.1002/2015MS000498

Bony, S., Stevens, B., Coppin, D., Becker, T., Reed, K. A., Voigt, A., & Medeiros, B. (2016). Thermodynamic Control of Anvil Cloud Amount. *Proceedings of the National Academy of Sciences of the United States of America*, *113*(32), 8927–8932. doi: 10.1073/pnas.1601472113

Bretherton, C. S., Blossey, P. N., & Khairoutdinov, M. (2005). An Energy-Balance Analysis of Deep Convective Self-Aggregation above Uniform SST. *Journal of the Atmospheric Sciences*, *62*(12), 4273–4292. doi: 10.1175/JAS3614.1

Bush, M., Allen, T., Bain, C., Boutle, I., Edwards, J., Finnenkoetter, A., ... Zerroukat, M. (2020). The first Met Office Unified Model-JULES Regional Atmosphere and Land configuration, RAL1. *Geoscientific Model Development*, *13*(4), 1999–2029. doi: 10.5194/gmd-13-1999-2020

Charney, J. G., & Phillips, N. A. (1953). Numerical Integration of the Quasi-Geostrophic Equations for Barotropic and Simple Baroclinic Flows. *Journal of the Atmospheric Sciences*, *10*(2), 71–99. doi: 10.1175/1520-0469(1953)010⟨0071:NIOTQG⟩2.0.CO;2

Coppin, D., & Bony, S. (2018). On the Interplay Between Convective Aggregation, Surface Temperature Gradients, and Climate Sensitivity. *Journal of Advances in Modeling Earth Systems*, *10*(12), 3123–3138. doi: 10.1029/2018MS001406

Edwards, J. M., & Slingo, A. (1996). Studies with a flexible new radiation code. I: Choosing a configuration for a large-scale model. *Quarterly Journal of the Royal Meteorological Society*, *122*(531), 689–719. doi: 10.1002/qj.49712253107

Emanuel, K., Wing, A. A., & Vincent, E. M. (2014). Radiative-Convective Instability. *Journal of Advances in Modeling Earth Systems*, *6*, 75-90. doi: 10.1002/2013MS000270

Held, I. M., Helmer, R. S., & Ramaswamy, V. (1993). Radiative-Convective Equilibrium with Explicit Two-Dimensional Moist Convection. *Journal of the Atmospheric Sciences*, *50*(23), 3909–3927. doi: 10.1175/1520-0469(1993)050⟨3909:RCEWET⟩2.0.CO;2

Hill, P. G., Allan, R. P., Chiu, J. C., Bodas-Salcedo, A., & Knippertz, P. (2018). Quantifying the Contribution of Different Cloud Types to the Radiation Budget in Southern West Africa. *Journal of Climate*, *31*(13), 5273–5291. doi: 10.1175/JCLI-D-17-0586.1

Holloway, C. E., Wing, A. A., Bony, S., Muller, C., Masunaga, H., L'Ecuyer, T. S., ... Zuidema, P. (2017). Observing Convective Aggregation. *Surveys in Geophysics*, *38*(6), 1199–1236. doi: 10.1007/s10712-017-9419-1

Holloway, C. E., & Woolnough, S. J. (2016). The Sensitivity of Convective Aggregation to Diabatic Processes in Idealized Radiative-Convective Equilibrium simulations. *Journal of Advances in Modeling Earth Systems*, *8*, 166–195. doi: 10.1002/2015MS000511

Houze, R. A. (2004). Mesoscale Convective Systems. *Reviews of Geophysics*, *42*(4), RG4003. doi: 10.1029/2004RG000150

Kiladis, G. N., Wheeler, M. C., Haertel, P. T., Straub, K. H., & Roundy, P. E. (2009). Convectively Coupled Equatorial Waves. *Reviews of Geophysics*, *47*(2),

RG2003. doi: 10.1029/2008RG000266

Lock, A. P., Brown, A. R., Bush, M. R., Martin, G. M., & Smith, R. N. B. (2000). A New Boundary Layer Mixing Scheme. Part I: Scheme Description and Single-Column Model Tests. *Monthly Weather Review*, *128*(9), 3187–3199. doi: 10.1175/1520-0493(2000)128⟨3200:ANBLMS⟩2.0.CO;2

Madden, R. A., & Julian, P. R. (1971). Detection of a 40–50 Day Oscillation in the Zonal Wind in the Tropical Pacific. *Journal of the Atmospheric Sciences*, *28*(5), 702–708. doi: 10.1175/1520-0469(1971)028⟨0702:DOADOI⟩2.0.CO;2

Mapes, B. E., & Houze, R. A. (1993). Cloud Clusters and Superclusters over the Oceanic Warm Pool. *Monthly Weather Review*, *121*(5), 1398-1415. doi: 10 .1175/1520-0493(1993)121⟨1398:CCASOT⟩2.0.CO;2

Morcrette, C. (2013). Sub-grid cloud parametrization issues in the met office unified model: A tale of several grey zones..

Muller, C., & Bony, S. (2015). What favors convective aggregation and why? *Geophysical Research Letters*, *42*(13), 5626–5634. doi: 10.1002/2015GL064260

Muller, C., & Held, I. M. (2012). Detailed Investigation of the Self-Aggregation of Convection in Cloud-Resolving Simulations. *Journal of the Atmospheric Sciences*, *69*(8), 2551–2565. doi: 10.1175/JAS-D-11-0257.1

Nakazawa, T. (1988). Tropical Super Clusters within Intraseasonal Variations over the Western Pacific. *Journal of the Meteorological Society of Japan*, *66*(6), 823–839. doi: 10.2151/jmsj1965.66.6_823

Smagorinsky, J. (1963). General Circulation Experiments with the Primitive Equations I. The Basic Experiment. *Monthly Weather Review*, *91*(3), 99–164. doi: 10.1175/1520-0493(1963)091⟨0099:GCEWTP⟩2.3.CO;2

Smith, R. N. (1990). A scheme for predicting layer clouds and their water content in a general circulation model. *Quarterly Journal of the Royal Meteorological Society*, *116*(492), 435–460. doi: 10.1002/qj.49711649210

Vaquero-Martínez, J., Antón, M., Ortiz de Galisteo, J. P., Román, R., & Cachorro, V. E. (2018). Water vapor radiative effects on short-wave radiation in Spain. *Atmospheric Research*, *205*, 18–25. doi: 10.1016/j.atmosres.2018.02.001

Walters, D., Baran, A. J., Boutle, I., Brooks, M., Earnshaw, P., Edwards, J., ... Zerroukat, M. (2019). The Met Office Unified Model Global Atmosphere 7.0/7.1 and JULES Global Land 7.0 configurations. *Geoscientific Model Development*, *12*(5), 1909–1963. doi: 10.5194/gmd-12-1909-2019

Wilson, D. R., & Ballard, S. P. (1999). A microphysically based precipitation scheme for the UK Meteorological Office Unified Model. *Quarterly Journal of the Royal Meteorological Society*, *125*(557), 1607–1636. doi: 10.1002/qj.49712555707

Wilson, D. R., Bushell, A. C., Kerr-Munslow, A. M., Price, J. D., & Morcrette, C. J. (2008). PC2: A prognostic cloud fraction and condensation scheme. I: Scheme description. *Quarterly Journal of the Royal Meteorological Society*, *134*(637), 2093–2107. doi: 10.1002/qj.333

Wing, A. A., & Cronin, T. W. (2016). Self-aggregation of convection in long channel geometry. *Quarterly Journal of the Royal Meteorological Society*, *142*(694), 1–15. doi: 10.1002/qj.2628

Wing, A. A., Emanuel, K., Holloway, C. E., & Muller, C. (2017). Convective Self-Aggregation in Numerical Simulations: A Review. *Surveys in Geophysics*, *38*(6), 1173–1197. doi: 10.1007/s10712-017-9408-4

Wing, A. A., & Emanuel, K. A. (2014). Physical Mechanisms Controlling Self-Aggregation of Convection in Idealized Numerical Modeling Simulations. *Journal of Advances in Modeling Earth Systems*, *6*(1), 59–74. doi: 10.1002/2013MS000269

Wing, A. A., Reed, K. A., Satoh, M., Stevens, B., Bony, S., & Ohno, T. (2018). Radiative-Convective Equilibrium Model Intercomparison Project. *Geoscientific Model Development*, *11*(2), 793–813. doi: 10.5194/gmd-11-793-2018

Wing, A. A., Stauffer, C. L., Becker, T., Reed, K. A., Ahn, M.-s., Arnold, N., ... Silvers, L. (2020). Clouds and Convective Self-Aggregation in a Multi-Model Ensemble of Radiative-Convective Equilibrium Simulations. *Journal of Advances in Modeling Earth Systems*, *12*(9), e2020MS0021380. doi: 10.1029/2020MS0021380,

Wood, N., Staniforth, A., White, A., Allen, T., Diamantakis, M., Gross, M., ... Thuburn, J. (2014). An inherently mass-conserving semi-implicit semi-Lagrangian discretization of the deep-atmosphere global non-hydrostatic equations. *Quarterly Journal of the Royal Meteorological Society*, *140*(682), 1505–1520. doi: 10.1002/qj.2235

Appendix A Normalized FMSE Variance Budget Equation Derivation

Starting with the equation of normalized FMSE:

$$\widehat{h}_n = \frac{\widehat{h} - \widehat{h}_{min}}{\widehat{h}_{max} - \widehat{h}_{min}} \tag{A1}$$

$\hat{h}_n$, can be broken down into its domain-mean state plus the anomaly from the mean:

$$\widehat{h}_n = \{\widehat{h}_n\} + \widehat{h}'_n \tag{A2}$$

where curly brackets denote the domain-mean state. Using this expansion of $\hat{h}_n$, equation A2 becomes:

$$\{\widehat{h}_n\} + \widehat{h}'_n = \frac{\{\hat{h}\} - \widehat{h}_{min}}{\widehat{h}_{max} - \widehat{h}_{min}} + \frac{\hat{h}'}{\widehat{h}_{max} - \widehat{h}_{min}} \tag{A3}$$

The first term on both sides of the equation is the domain-mean of $\widehat{h}_n$ and the second term is the anomaly. By subtracting the domain-mean from this equation, we end up with an expression for the anomaly of $\widehat{h}_n$:

$$\widehat{h}'_n = \frac{\hat{h}'}{\widehat{h}_{max} - \widehat{h}_{min}} \tag{A4}$$

Differentiating this with respect to time:

$$\frac{\partial \widehat{h}'_n}{\partial t} = \frac{1}{\widehat{h}_{max} - \widehat{h}_{min}} \frac{\partial \widehat{h}'}{\partial t} \tag{A5}$$

Multiplying through by $\widehat{h}'_n$, using the identity $x \times \partial x/\partial t = 1/2 \times \partial x^2/\partial t$ on the left hand side, and substituting equation (A4) for $\widehat{h}'_n$ on the right hand side:

$$\frac{1}{2}\frac{\partial \widehat{h}'^2_n}{\partial t} = \frac{\widehat{h}'}{(\widehat{h}_{max} - \widehat{h}_{min})^2} \frac{\partial \widehat{h}'}{\partial t} \tag{A6}$$

Taking the anomaly of the expression for the tendency of $\widehat{h}$ shown in equation 3 of Wing and Emanuel (2014):

$$\frac{\partial \widehat{h}'}{\partial t} = SEF' + LW' + SW' - \nabla_h . \mathbf{u}\hat{h} \tag{A7}$$

Substituting this into equation (A6) gives us an expression for the $\widehat{h}_n$ tendency budget in terms of $\hat{h}'$:

$$\frac{1}{2}\frac{\partial \widehat{h}_n'^2}{\partial t} = \frac{\hat{h}'LW' + \hat{h}'SW' + \hat{h}'SEF' - \hat{h}'\nabla_h . \mathbf{u}\hat{h}}{(\widehat{h}_{max} - \widehat{h}_{min})^2} \tag{A8}$$

Or in terms of $\hat{h}'_n$, the equation becomes:

$$\frac{1}{2}\frac{\partial \widehat{h}_n'^2}{\partial t} = \hat{h}'_n LW'_n + \hat{h}'_n SW'_n + \hat{h}'_n SEF'_n - \hat{h}'_n \nabla_h . \mathbf{u}\hat{h}_n \tag{A9}$$

Here, each normalized variable is equal to the original variable in equation 3 divided by the difference between $\widehat{h}_{max}$ and $\widehat{h}_{min}$.

Figure 1.pdf.

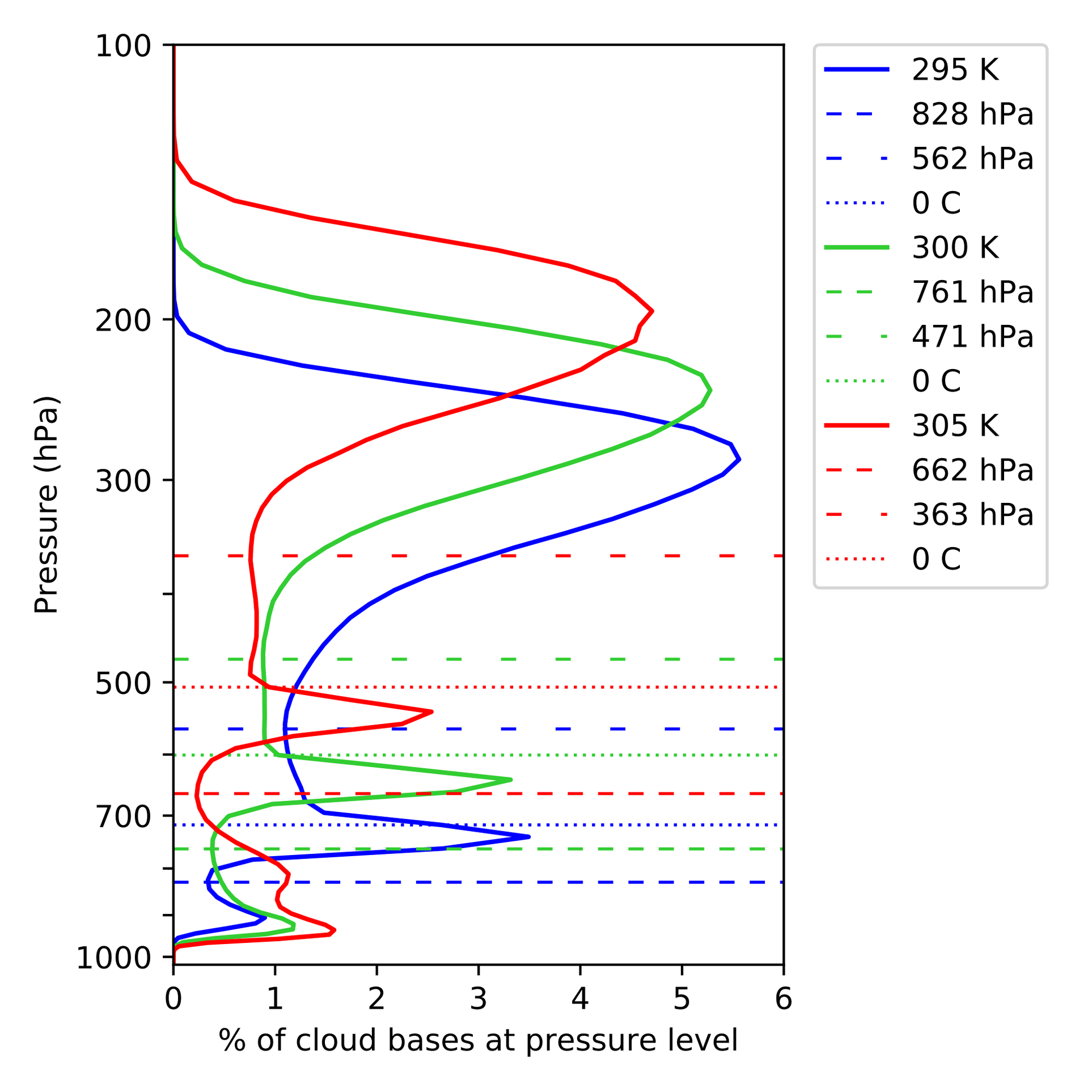
100
200
300
500
700
1000
Pressure (hPa)
0
1
2
3
4
5
6
% of cloud bases at pressure level
295 K
828 hPa
562 hPa
0 C
300 K
761 hPa
471 hPa
0 C
305 K
662 hPa
363 hPa
0 C

Figure 2.jpg.

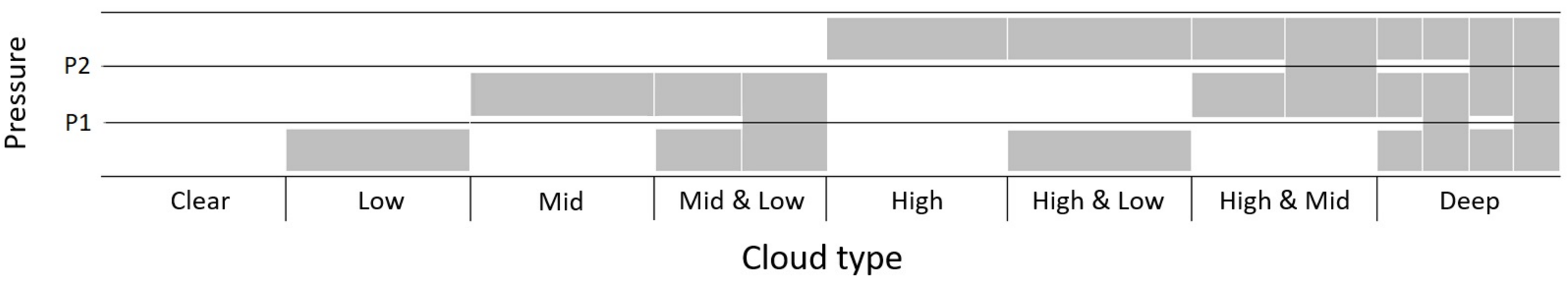
Pressure
P2
P1
Clear
Low
Mid
Mid & Low
High
High & Low
High & Mid
Deep
Cloud type

Figure 3.pdf.

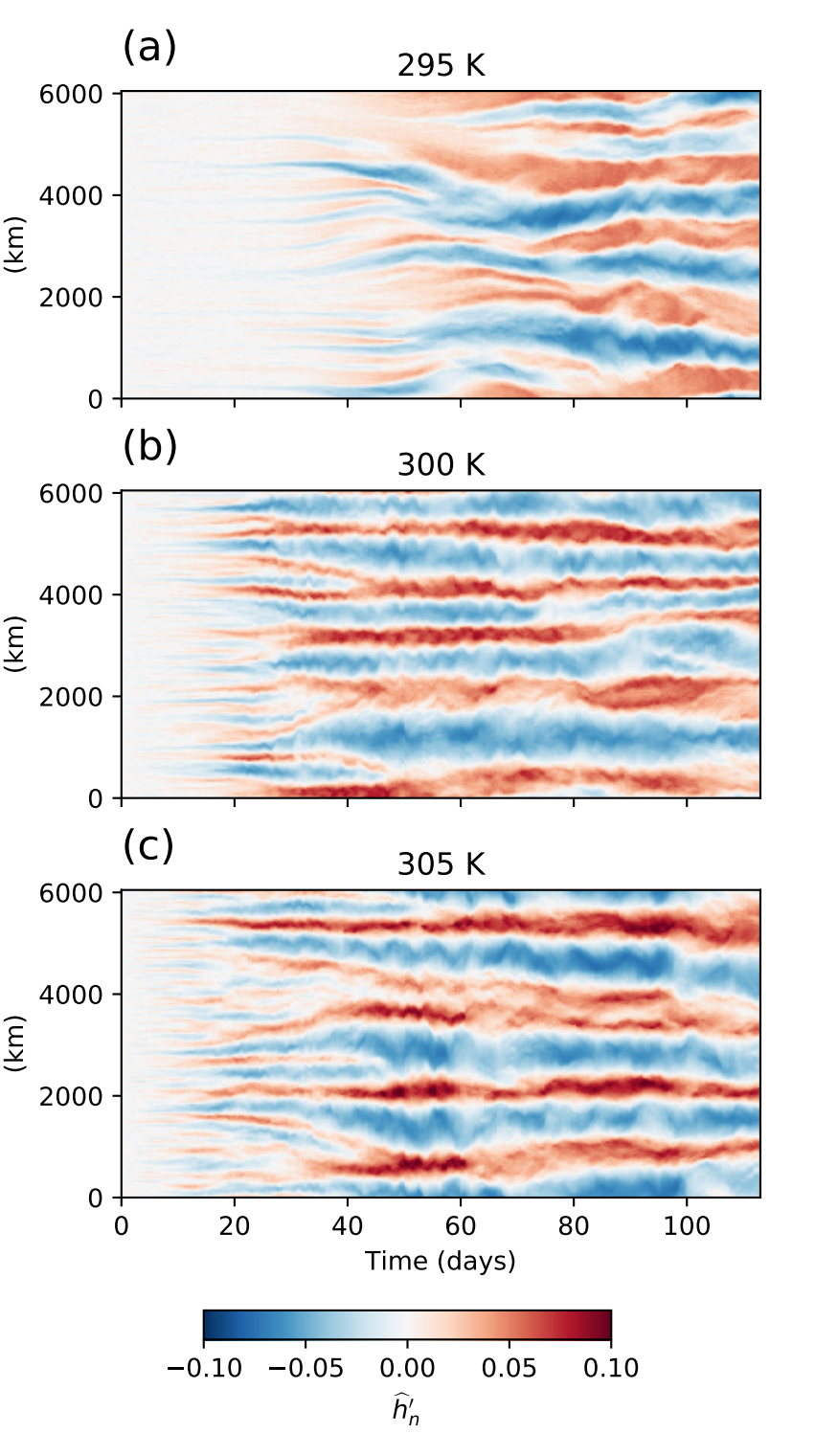
(a)
295 K
(b)
300 K
(c)
305 K
6000
4000
2000
0
(km)
0
20
40
60
80
100
Time (days)
−0.10
−0.05
0.00
0.05
0.10
$\widehat{h}'_n$

Figure 4.pdf.

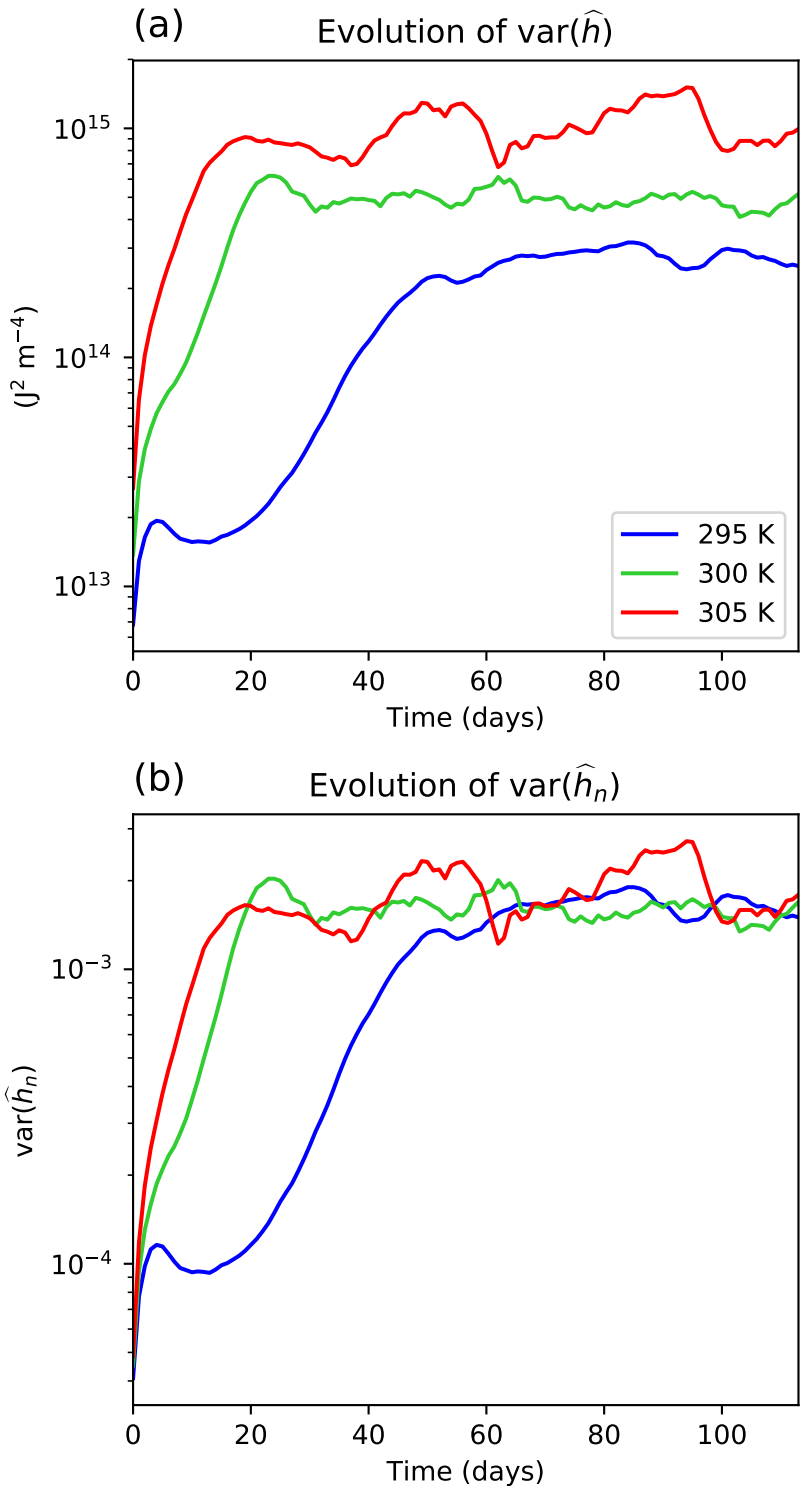
(a)
Evolution of var($\widehat{h}$)
10^{15}
10^{14}
10^{13}
(J^2 m^{-4})
295 K
300 K
305 K
0
20
40
60
80
100
Time (days)
(b)
Evolution of var($\widehat{h}_n$)
10^{-3}
10^{-4}
var($\widehat{h}_n$)
0
20
40
60
80
100
Time (days)

Figure 5.pdf.

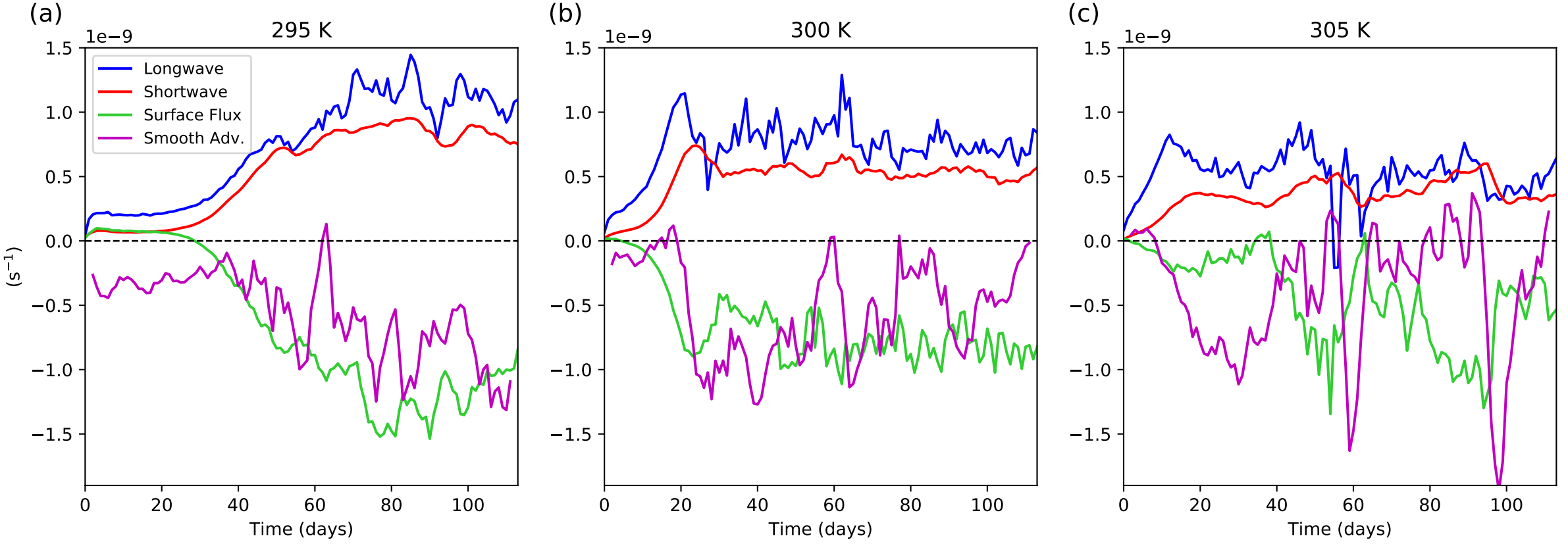
(a)
295 K
1e−9
Longwave
Shortwave
Surface Flux
Smooth Adv.
(s^{-1})
Time (days)
(b)
300 K
1e−9
Time (days)
(c)
305 K
1e−9
Time (days)

Figure 6.pdf.

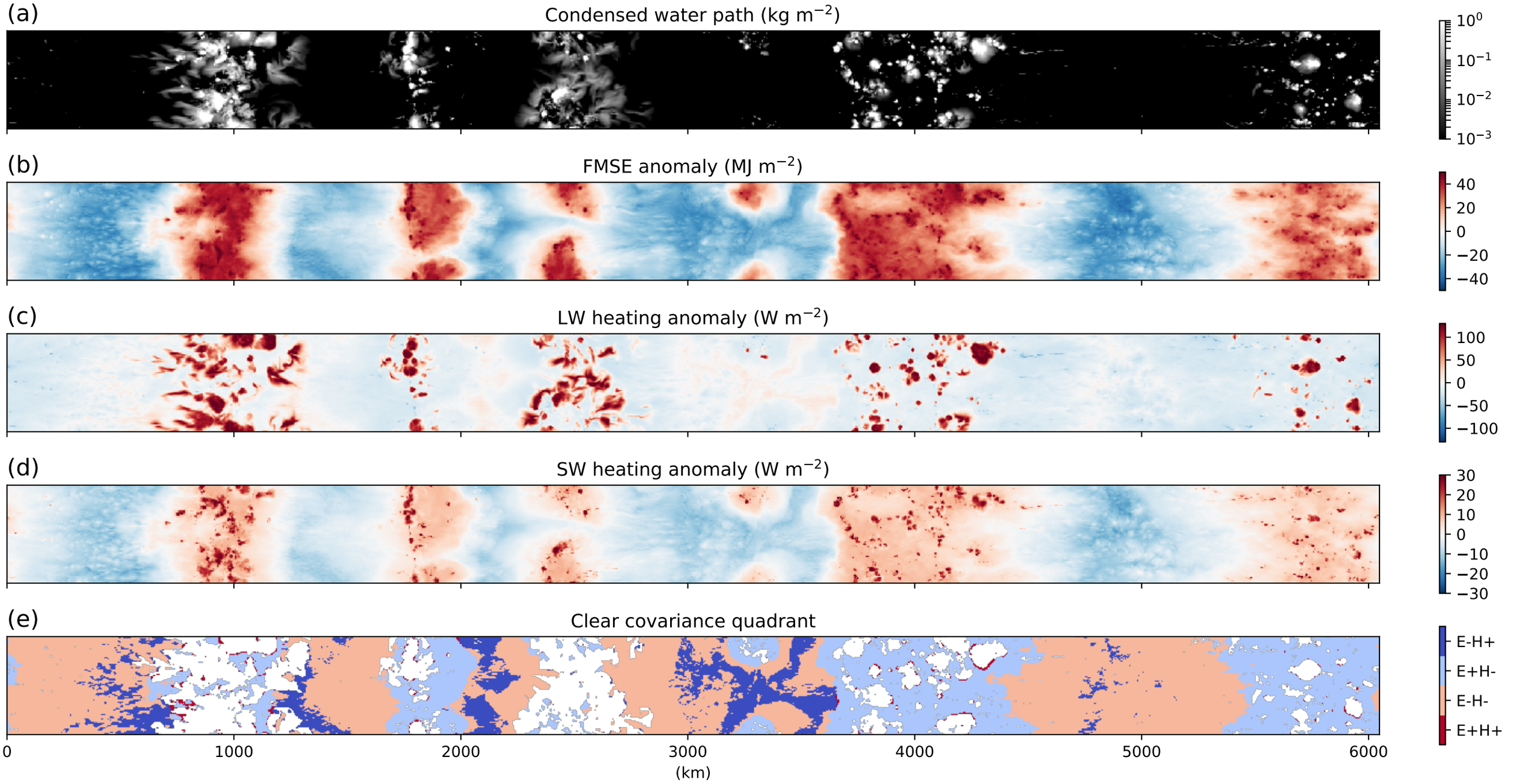
(a)
Condensed water path (kg m^{-2})
10^{0}
10^{-1}
10^{-2}
10^{-3}
(b)
FMSE anomaly (MJ m^{-2})
40
20
0
−20
−40
(c)
LW heating anomaly (W m^{-2})
100
50
0
−50
−100
(d)
SW heating anomaly (W m^{-2})
30
20
10
0
−10
−20
−30
(e)
Clear covariance quadrant
E-H+
E+H-
E-H-
E+H+
0
1000
2000
3000
4000
5000
6000
(km)

Figure 7.pdf.

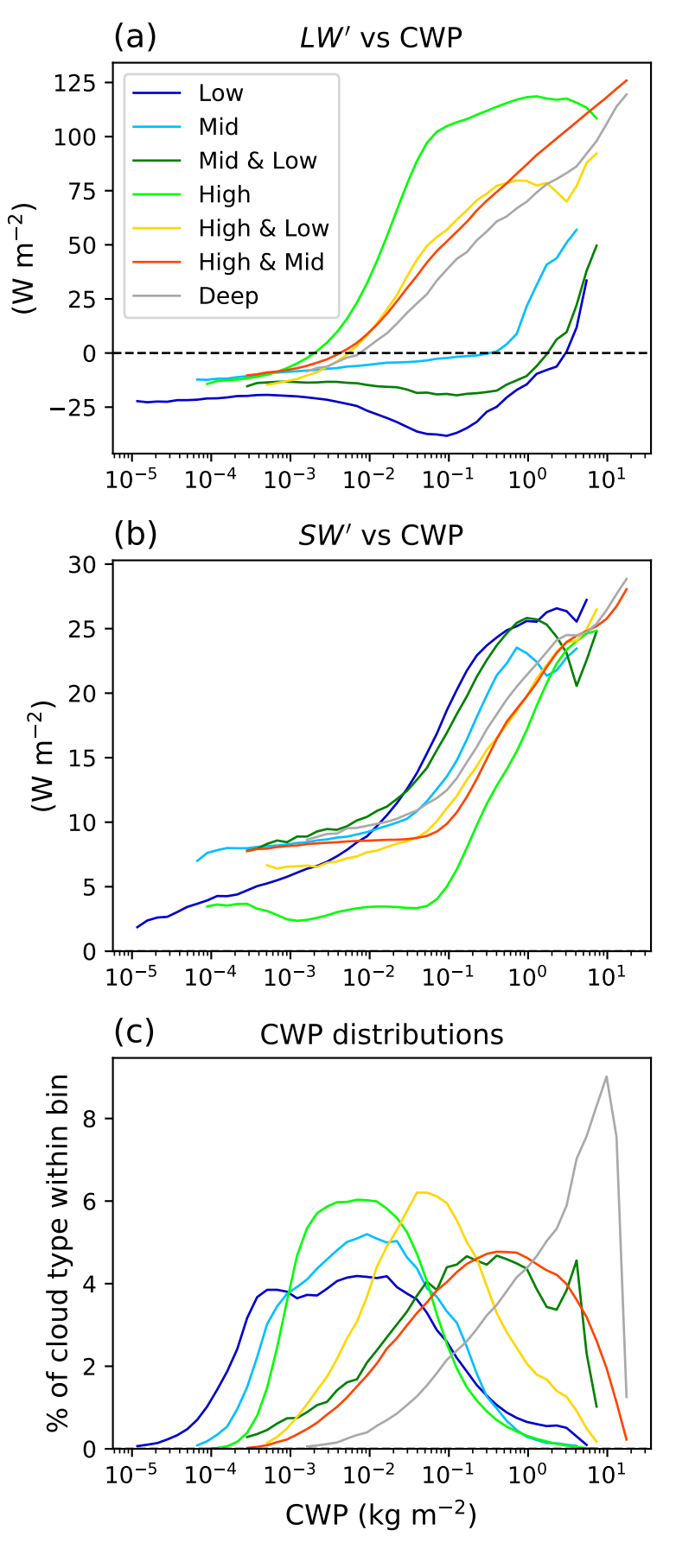
(a)
LW′ vs CWP
Low
Mid
Mid & Low
High
High & Low
High & Mid
Deep
(W m−2)
125
100
75
50
25
0
−25
10−5
10−4
10−3
10−2
10−1
100
101
(b)
SW′ vs CWP
(W m−2)
30
25
20
15
10
5
0
(c)
CWP distributions
% of cloud type within bin
8
6
4
2
0
CWP (kg m−2)

Figure 8.pdf.

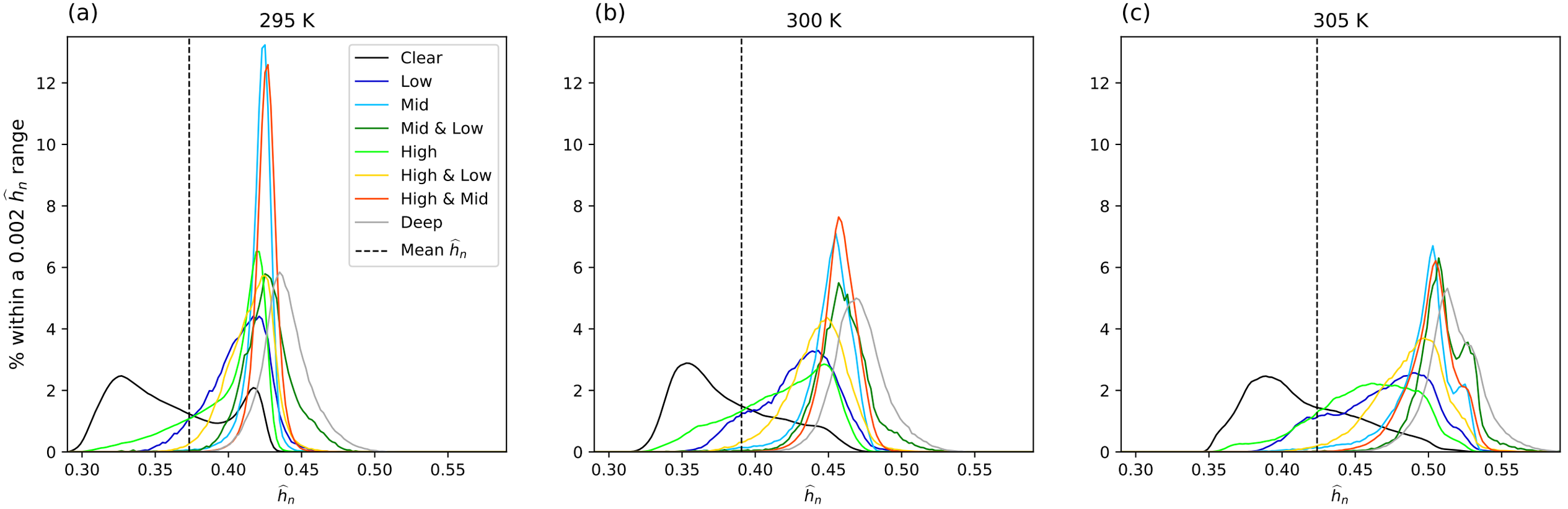
(a)
295 K
(b)
300 K
(c)
305 K
% within a 0.002 $\widehat{h}_n$ range
$\widehat{h}_n$
Clear
Low
Mid
Mid & Low
High
High & Low
High & Mid
Deep
Mean $\widehat{h}_n$
0
2
4
6
8
10
12
0.30
0.35
0.40
0.45
0.50
0.55

Figure 9.pdf.

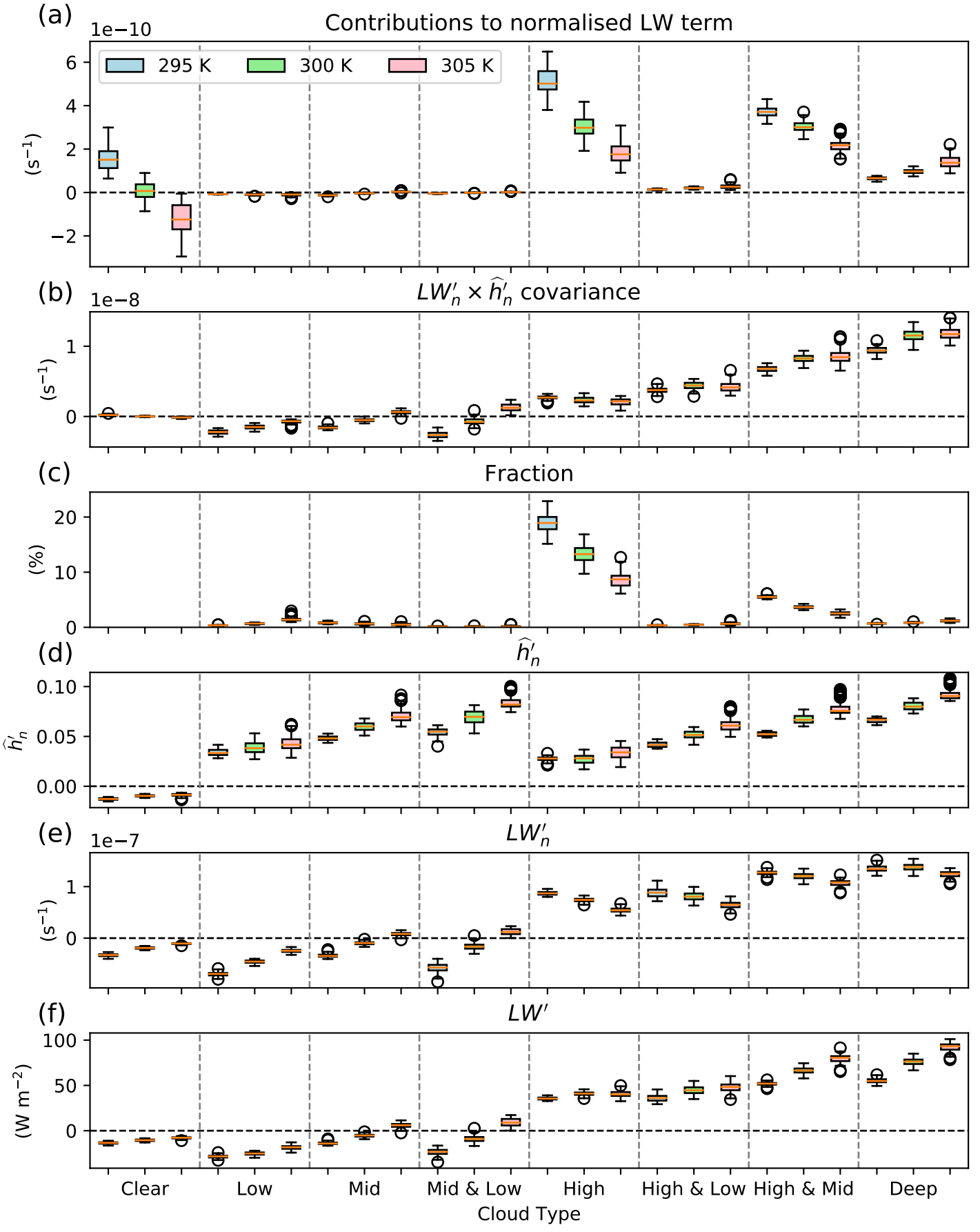
(a)
Contributions to normalised LW term
1e−10
295 K
300 K
305 K
(s^{-1})
(b)
$LW'_n \times \widehat{h}'_n$ covariance
1e−8
(s^{-1})
(c)
Fraction
(%)
(d)
$\widehat{h}'_n$
$\widehat{h}'_n$
(e)
LW'_n
1e−7
(s^{-1})
(f)
LW'
(W m^{-2})
Clear
Low
Mid
Mid & Low
High
High & Low
High & Mid
Deep
Cloud Type

Figure 10.pdf.

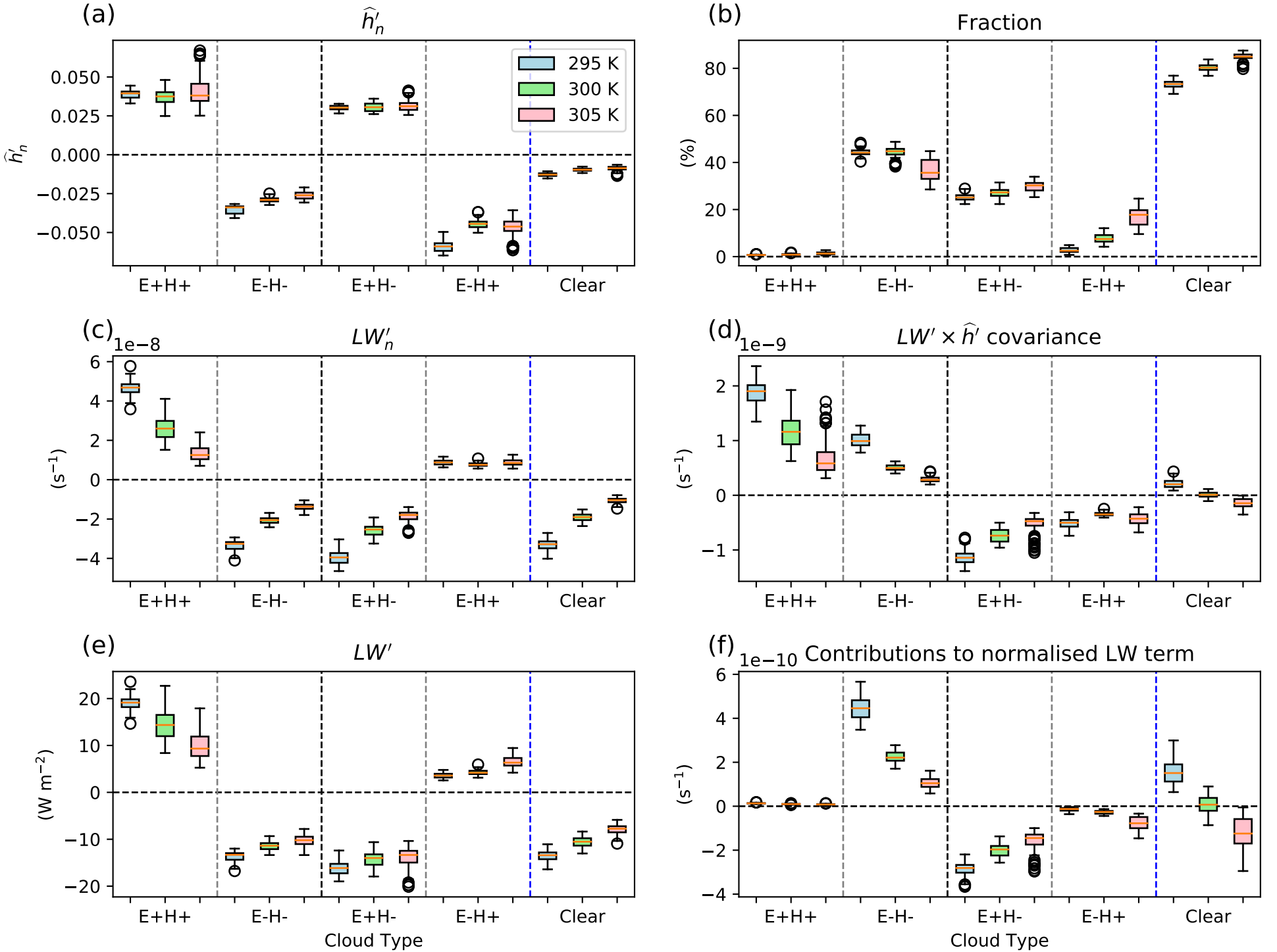
(a)
$\widehat{h}'_n$
295 K
300 K
305 K
$\widehat{h}'_n$
0.050
0.025
0.000
−0.025
−0.050
E+H+
E-H-
E+H-
E-H+
Clear
(b)
Fraction
(%)
80
60
40
20
0
(c)
1e−8
LW'_n
(s^{-1})
6
4
2
0
−2
−4
(d)
1e−9
$LW' \times \widehat{h}'$ covariance
(s^{-1})
2
1
0
−1
(e)
LW'
(W m^{-2})
20
10
0
−10
−20
(f)
1e−10 Contributions to normalised LW term
(s^{-1})
6
4
2
0
−2
−4
Cloud Type

Figure 11.pdf.

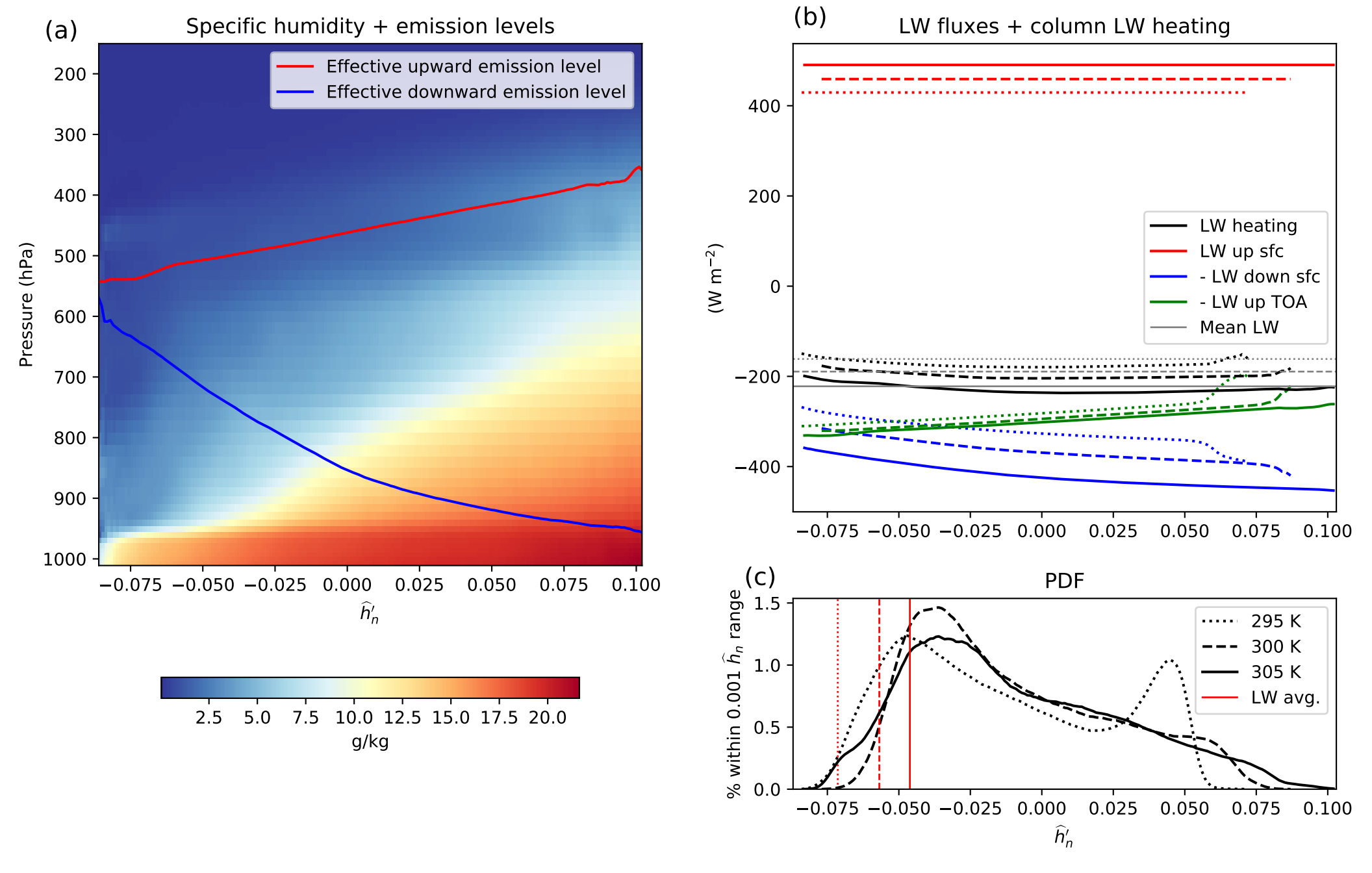
(a)
Specific humidity + emission levels
Effective upward emission level
Effective downward emission level
Pressure (hPa)
200
300
400
500
600
700
800
900
1000
−0.075 −0.050 −0.025 0.000 0.025 0.050 0.075 0.100
$\widehat{h}'_n$
2.5 5.0 7.5 10.0 12.5 15.0 17.5 20.0
g/kg
(b)
LW fluxes + column LW heating
(W m^{-2})
400
200
0
−200
−400
LW heating
LW up sfc
- LW down sfc
- LW up TOA
Mean LW
−0.075 −0.050 −0.025 0.000 0.025 0.050 0.075 0.100
(c)
PDF
% within 0.001 $\widehat{h}_n$ range
1.5
1.0
0.5
0.0
295 K
300 K
305 K
LW avg.
−0.075 −0.050 −0.025 0.000 0.025 0.050 0.075 0.100
$\widehat{h}'_n$

Figure 12.pdf.

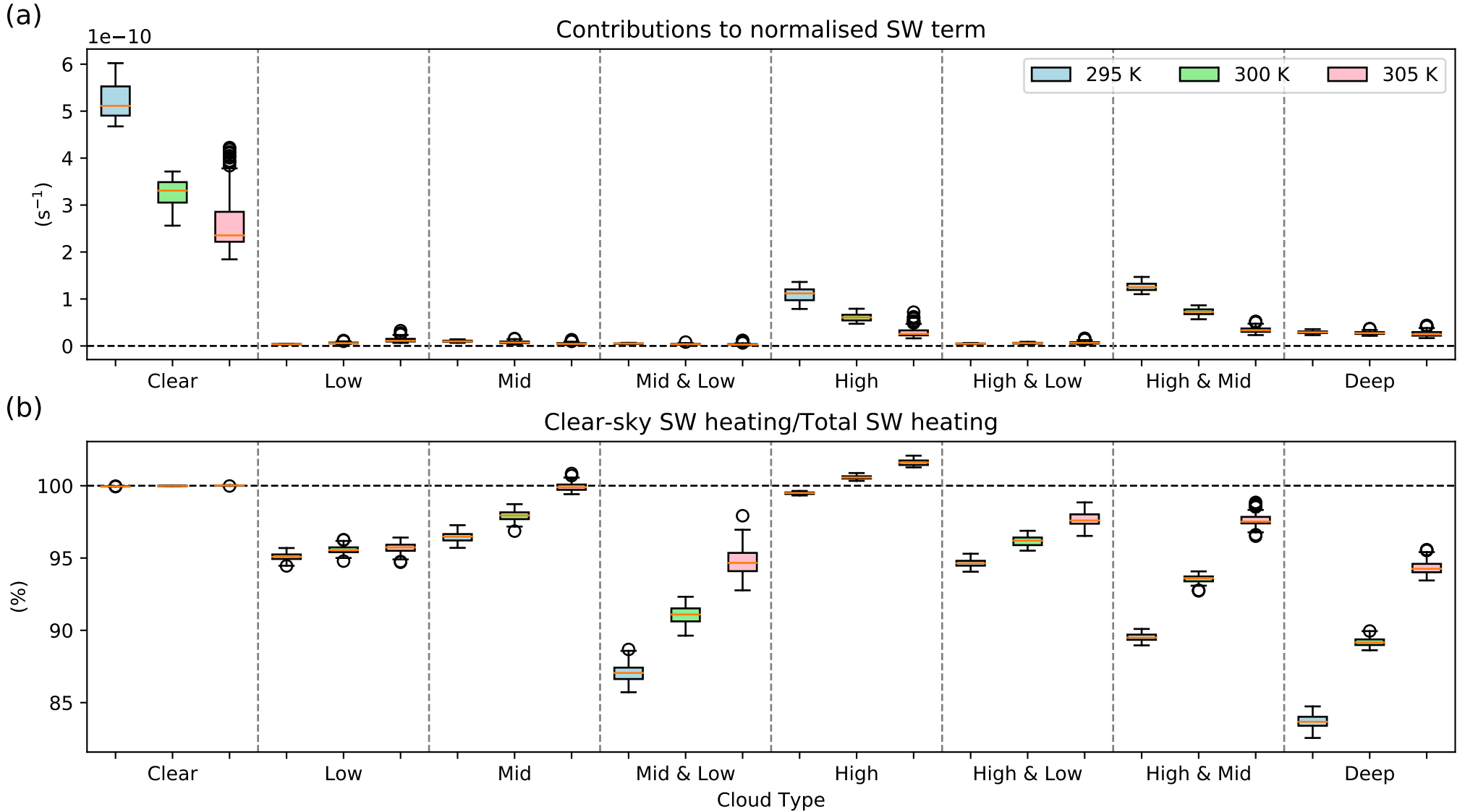
(a)
Contributions to normalised SW term
1e−10
6
5
4
3
2
1
0
(s^{-1})
295 K
300 K
305 K
Clear
Low
Mid
Mid & Low
High
High & Low
High & Mid
Deep
(b)
Clear-sky SW heating/Total SW heating
100
95
90
85
(%)
Clear
Low
Mid
Mid & Low
High
High & Low
High & Mid
Deep
Cloud Type

Figure 13.pdf.

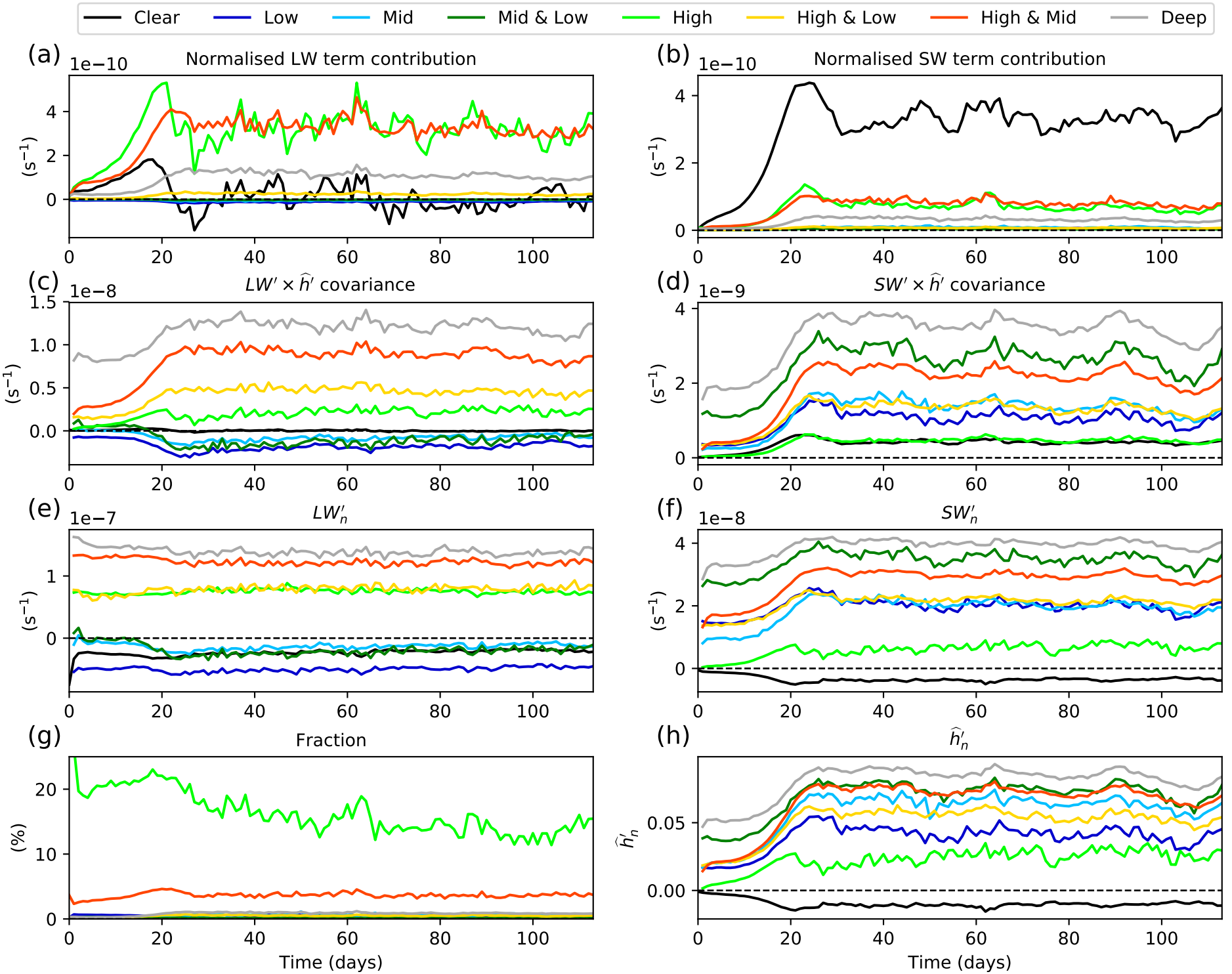
Clear
Low
Mid
Mid & Low
High
High & Low
High & Mid
Deep
(a)
Normalised LW term contribution
1e−10
(b)
Normalised SW term contribution
1e−10
(c)
$LW' \times \widehat{h}'$ covariance
1e−8
(d)
$SW' \times \widehat{h}'$ covariance
1e−9
(e)
LW'_n
1e−7
(f)
SW'_n
1e−8
(g)
Fraction
(%)
(h)
$\widehat{h}'_n$
(s^{-1})
Time (days)
Time (days)

Figure 14.pdf.

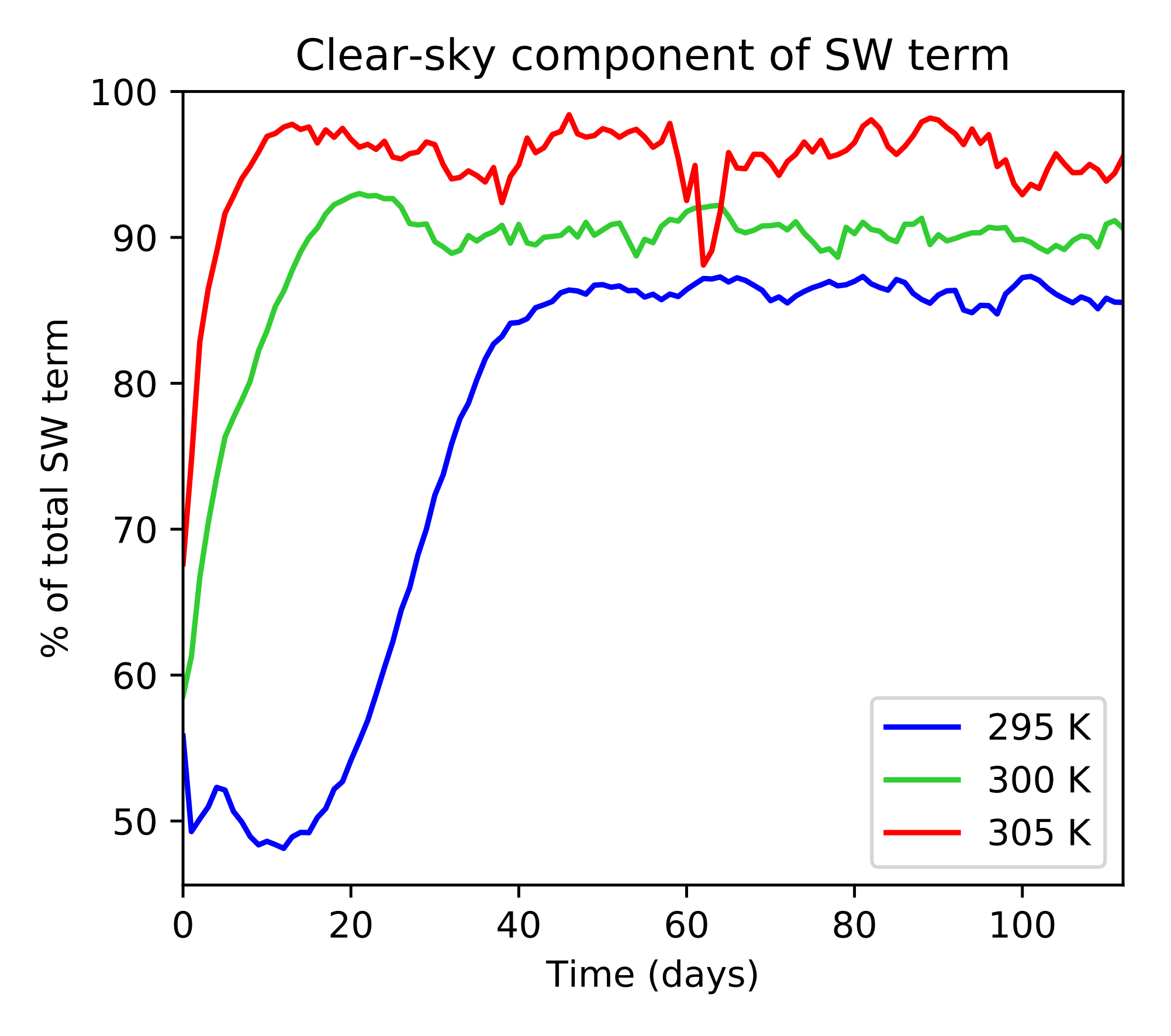
Clear-sky component of SW term
100
90
80
70
60
50
% of total SW term
0
20
40
60
80
100
Time (days)
295 K
300 K
305 K

Figure 15.pdf.

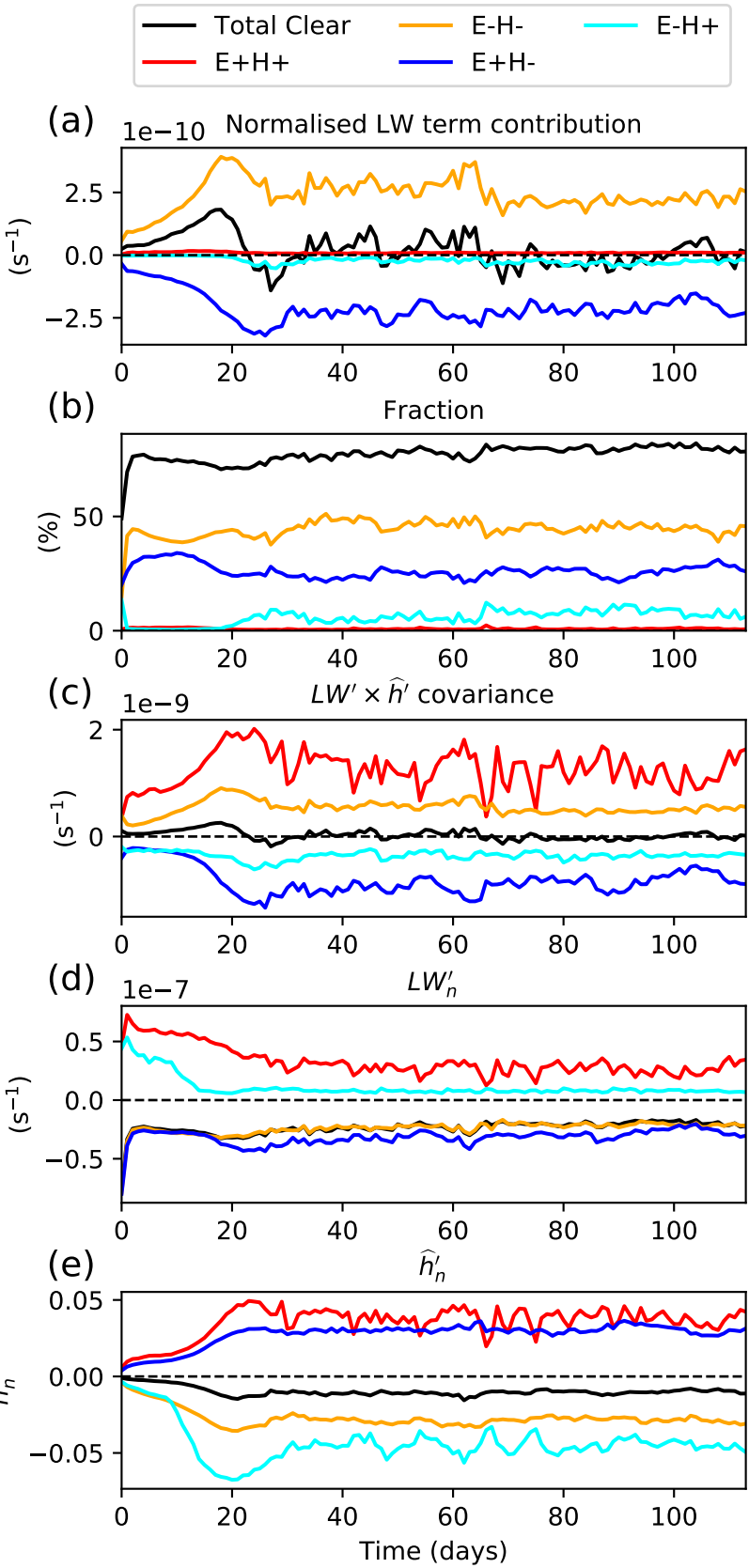
Total Clear
E+H+
E-H-
E+H-
E-H+
(a)
1e−10
Normalised LW term contribution
(s^{-1})
2.5
0.0
−2.5
0
20
40
60
80
100
(b)
Fraction
(%)
50
0
(c)
1e−9
$LW' \times \widehat{h}'$ covariance
(s^{-1})
2
0
(d)
1e−7
LW'_n
(s^{-1})
0.5
0.0
−0.5
(e)
$\widehat{h}'_n$
$\widehat{h}'_n$
0.05
0.00
−0.05
Time (days)

Figure 16.pdf.

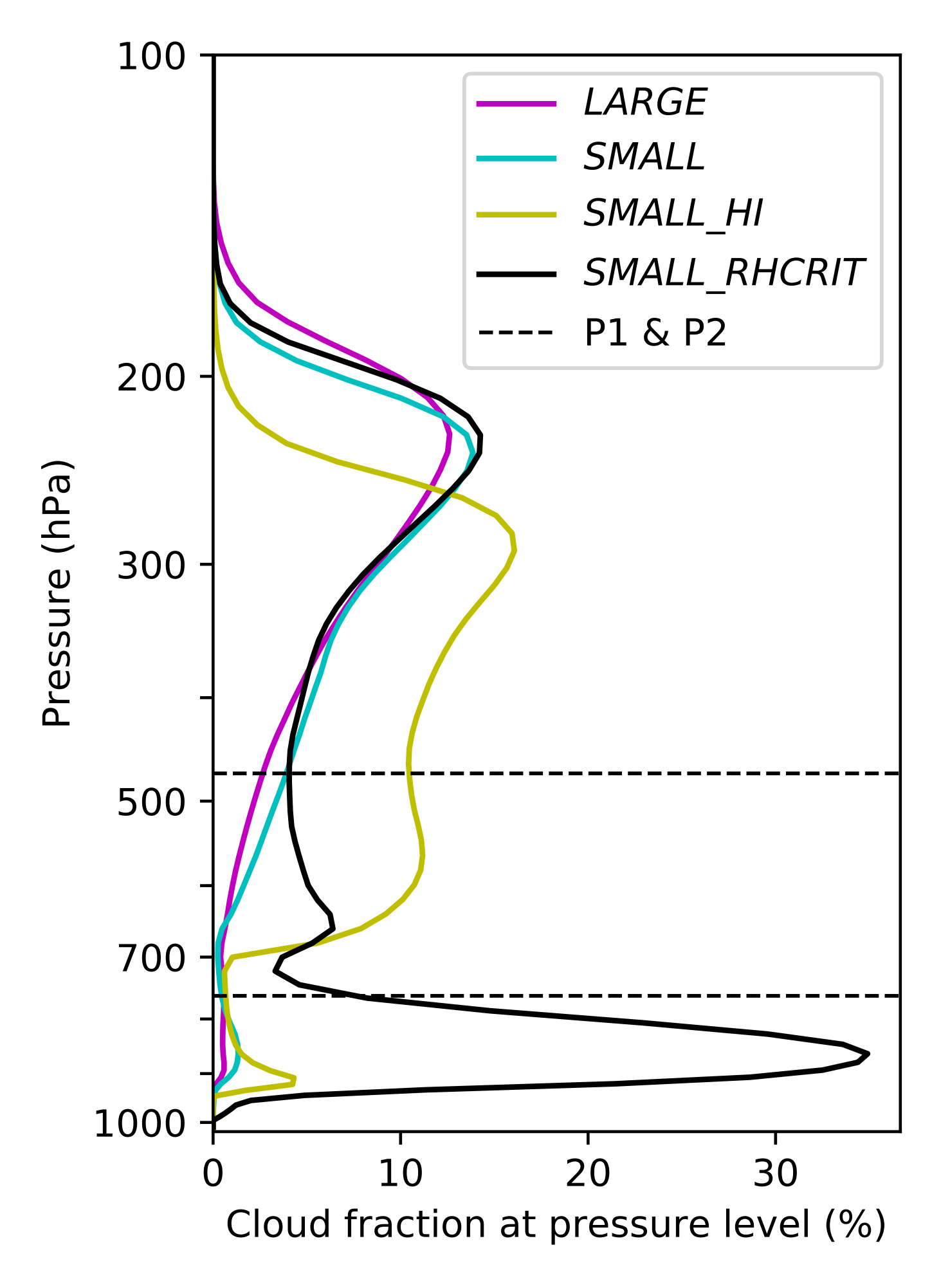
100
200
300
500
700
1000
Pressure (hPa)
0
10
20
30
Cloud fraction at pressure level (%)
LARGE
SMALL
SMALL_HI
SMALL_RHCRIT
P1 & P2

Figure 17.pdf.

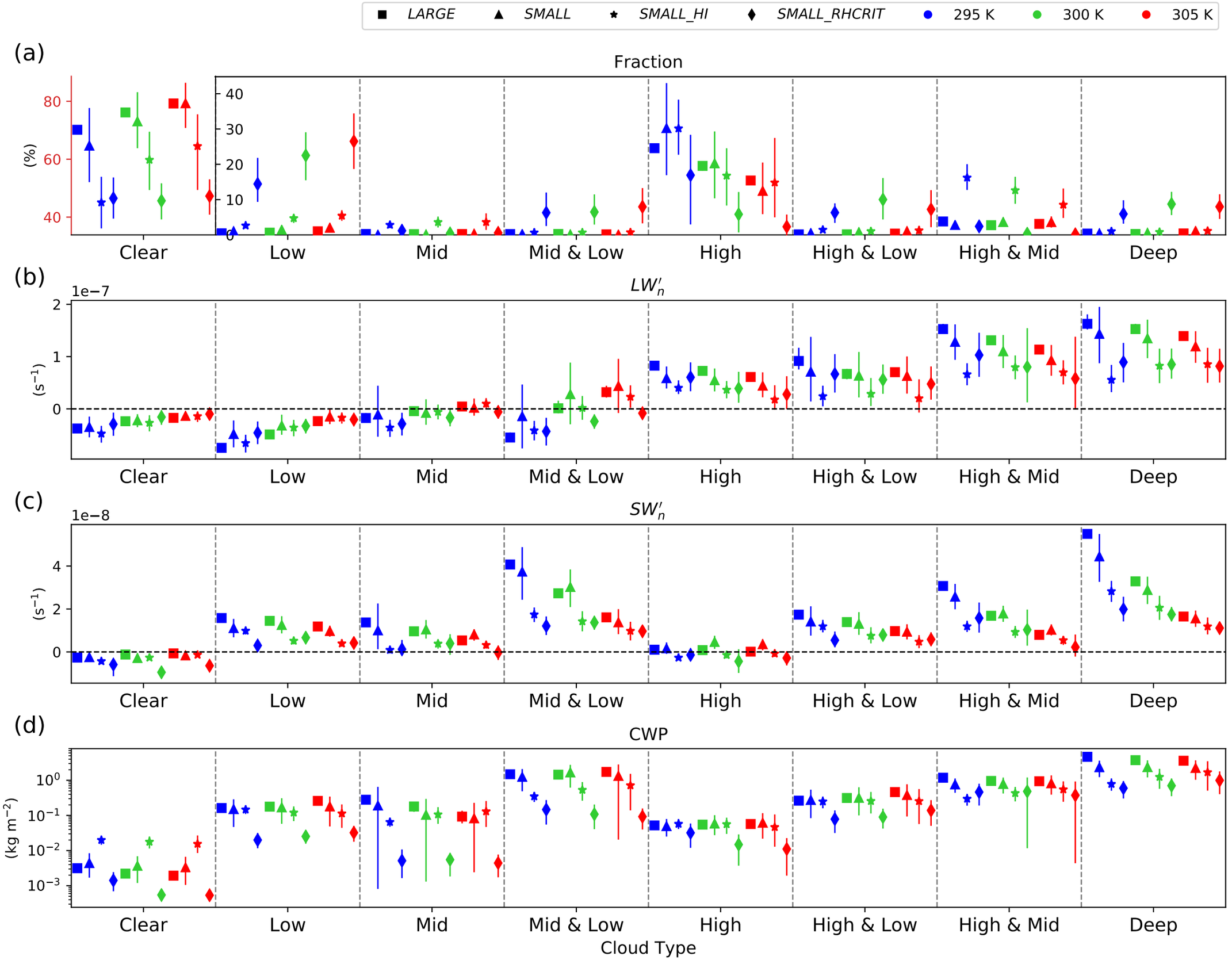
LARGE
SMALL
SMALL_HI
SMALL_RHCRIT
295 K
300 K
305 K
(a)
Fraction
(%)
80
60
40
40
30
20
10
0
Clear
Low
Mid
Mid & Low
High
High & Low
High & Mid
Deep
(b)
LW'_n
1e−7
(s^{-1})
2
1
0
(c)
SW'_n
1e−8
(s^{-1})
4
2
0
(d)
CWP
$(kg\ m^{-2})$
10^{0}
10^{-1}
10^{-2}
10^{-3}
Cloud Type